Nano Research Energy

ISSN 2791-0091 CN 10-1944/O6
https://doi.org/10.26599/NRE.2026.9120266

Review Article

Mechanistic insights and multiscale stabilization strategies for aqueous $LiFePO_4$ batteries

Jiaxin Hu[1,§], Liyu Du[2,§], Shang Gong[2], Chongze Ding[2], Menglei Yuan[3](✉), Meng Yao[2](✉)

[1] School of Materials Science and Engineering, Nanyang Technological University, Block N4.1, 50 Nanyang Avenue, 639798, Singapore

[2] College of Materials Science and Engineering, Sichuan University, Chengdu 610065, China

[3] State Key Laboratory of Solidification Processing and School of Materials Science and Engineering, Northwestern Polytechnical University, Xi'an 710072, China

[§] Jiaxin Hu and Liyu Du contributed equally to this work.

Nano Research Energy, **Just Accepted Manuscript** • https://doi.org/10.26599/NRE.2026.9120266

https://www.sciopen.com/journal/2791-0091 on Aug. 14, 2026

Just Accepted

TABLE OF CONTENTS (TOC)

Mechanistic Insights and Multiscale Stabilization Strategies for Aqueous $LiFePO_4$ Batteries

Jiaxin Hu[1], Liyu Du[2], Shang Gong[2], Chongze Ding[2], Menglei Yuan[3,*], Meng Yao[2,*]

[1]Nanyang Technological University, Singapore
[2]Sichuan University, China
[3]Northwestern Polytechnical University, China

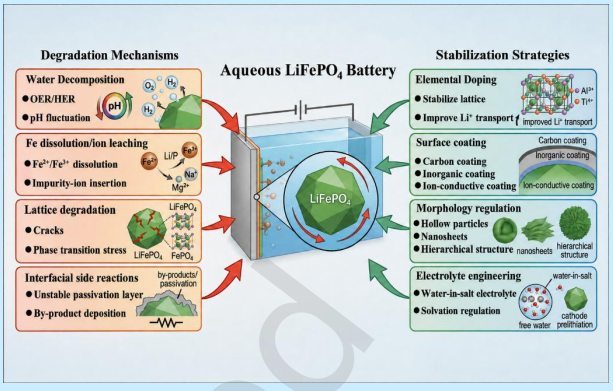

This review highlights the coupled degradation pathways and multiscale stabilization strategies of $LiFePO_4$ cathodes in aqueous batteries, providing guidance for the design of long-life and high-safety aqueous energy-storage systems.

Nano Research Energy

ISSN 2791-0091 (print); 2790-8119 (online)
https://doi.org/10.26599/NRE.2026.9120266

Review Article

Mechanistic insights and multiscale stabilization strategies for aqueous $LiFePO_4$ batteries

Jiaxin Hu[1,§], Liyu Du[2,§], Shang Gong[2], Chongze Ding[2], Menglei Yuan[3] (✉), and Meng Yao[2] (✉)

[1]School of Materials Science and Engineering, Nanyang Technological University, Block N4.1, 50 Nanyang Avenue, 639798 Singapore
[2]College of Materials Science and Engineering, Sichuan University, Chengdu 610065, China
[3]State Key Laboratory of Solidification Processing and School of Materials Science and Engineering, Northwestern Polytechnical University, Xi'an 710072, China
[§]Jiaxin Hu and Liyu Du contributed equally to this work.

Received: 29 June 2026 / **Revised:** 27 July 2026 / **Accepted:** 3 August 2026

ABSTRACT

Lithium iron phosphate ($LiFePO_4$, LFP) is regarded as a promising cathode material for aqueous lithium-ion batteries (ALIBs) due to its excellent structural stability and intrinsic safety. However, when operated in aqueous electrolytes, LFP suffers from more severe capacity decay and poorer cycling stability than those in non-aqueous systems. Recent studies have revealed that LFP degradation in aqueous system arises from several coupled processes, including electrolyte decomposition at high potentials, Fe dissolution and impurity-ion intercalation, lattice distortion during repeated Li^+ insertion/extraction, and unstable interfacial passivation. Electrolyte decomposition induces local pH fluctuations and interfacial reconstruction, which exacerbate transition metal leaching and lattice degradation, the resulting structural defects and freshly exposed surfaces in turn accelerate further interfacial side reactions. These processes collectively lead to active-material loss, sluggish ion transport, and aggravated polarization. To address these failure pathways, this review summarizes current stabilization strategies, including elemental doping, surface coating, morphological regulation, and modification of electrolytes. The underlying mechanisms are analyzed from the perspectives of thermodynamic stability, interfacial kinetics, and solvation-structure regulation. Finally, future research directions, including in situ characterization, multiphysics coupled modeling, and low-cost electrolytes with high-salt effects, are discussed to provide guidance for the mechanism-driven design of high-performance aqueous cathode materials.

KEYWORDS

aqueous lithium-ion batteries, $LiFePO_4$ cathodes, degradation mechanisms, interfacial stabilization, electrolyte engineering

1 Introduction

In recent years, the demand for high-safety, low-cost green energy storage technologies has continuously increased across various fields, and aqueous lithium-ion batteries (ALIBs) have emerged due to advantages such as nonflammable electrolytes, low manufacturing costs, and environmental friendliness [1-6]. Recent studies have further emphasized that the practical performance of aqueous metal-ion batteries is governed not only by electrode chemistry but also by electrochemical-engineering factors, including ion transport through the electrolyte, interfacial diffusion, and electrode reaction kinetics, particularly under high-loading and thick-electrode condition [7]. Among numerous cathode materials, lithium iron phosphate ($LiFePO_4$, LFP) is considered one of the ideal cathodes for aqueous lithium-ion batteries due to its relatively high operating potential (vs. Li^+/Li), good structural stability, and selective lithium intercalation/deintercalation capability [8-9]. The basic working principle of LFP relies on the reversible intercalation and deintercalation of Li^+ between the cathode and anode to store and release energy. In novel highly concentrated electrolyte systems such as "water-in-salt," the electrochemical stability window of water is expanded, further enhancing the application potential of LFP in aqueous systems [10-12].

However, LFP exhibits rapid capacity decay and reduced cycling stability in aqueous electrolytes. During the charging process, the Fe^{2+}/Fe^{3+} redox reaction

Address correspondence to Menglei Yuan, mlyuan@nwpu.edu.cn; Meng Yao, yaomeng@scu.edu.cn

inevitably competes with the oxygen evolution reaction (OER), resulting in parasitic currents and decreased charge utilization efficiency [13-15]. OER-induced interfacial reactions further promote transition metal dissolution and lattice degradation, thereby forming a coupled degradation pathway involving potential overlap, side-reaction initiation, and structural instability [8;16-17]. This multi-process synergy significantly exacerbates the loss of active material and interfacial polarization, thereby limiting the capacity retention and long-term cycling performance of aqueous LFP batteries [18]. Moreover, studies have shown that the involvement of water molecules and protons (H^+) may trigger a series of complex structural degradation processes (Fig. 1) [19]. Hydration could cause crystal structure expansion and phase separation, while H^+ intercalation competes with Li^+, occupying diffusion channels and causing blockage of one-dimensional lithium-ion transport pathways [20-21]. Furthermore, Fe dissolution and migration during interfacial reactions may lead to by-product deposition, ultimately causing irreversible structural damage and capacity decay [22-23]. These processes together constitute the typical failure pathway of LFP in aqueous systems [24, 25].

Therefore, systematically reviewing the degradation mechanisms of LFP in aqueous electrolytes and summarizing targeted modification strategies for distinct failure pathways is of great significance for advancing high-performance, long-life aqueous lithium-ion batteries toward practical applications. This work outlines the key degradation behaviors of LFP in aqueous environments and elucidates the underlying failure mechanisms. Recent advances in material design, electrode-interface engineering, and electrolyte optimization are then critically evaluated to establish a comprehensive framework for aqueous LFP systems. This review provides mechanistic insights and multi-scale design guidelines for the rational development of high-stability aqueous $LiFePO_4$ batteries with extended cycling lifespan.

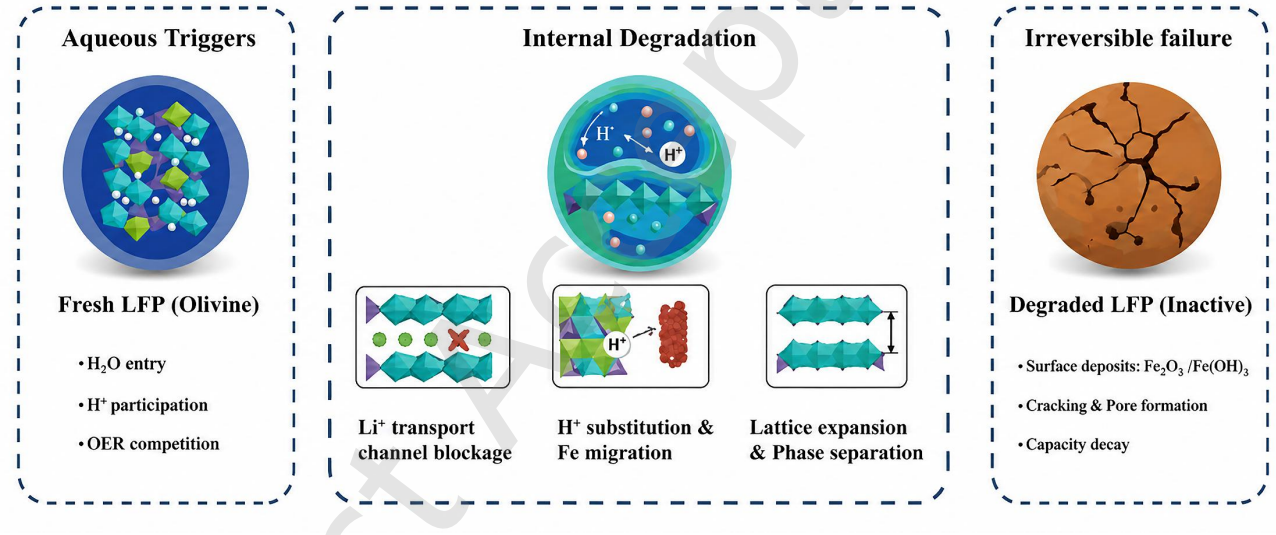

Figure 1 Schematic of the degradation mechanism of $LiFePO_4$ in aqueous environments.

2 Degradation Mechanisms of LFP in Aqueous Environments

Although LFP exhibits favorable electrochemical properties in aqueous batteries, its degradation is governed by coupled and co-evolving processes, including electrolyte decomposition, interfacial side reactions, transition-metal dissolution, and crystal-structure deterioration [26-27].

During the charge-discharge processes, the migration of Li^+ between the electrodes, accompanied by electron transport through the external circuit, inevitably triggers complex chemical reactions at the electrode/electrolyte interface [28-30]. On one hand, water decomposition at high potentials, particularly the oxygen evolution reaction (OER), induces local pH fluctuations, gas evolution, and continuous interfacial reconstruction, promoting Fe dissolution and by-product deposition on the LFP/FP surface [31]. On the other hand, anisotropic stress generated by repeated lithium insertion/extraction causes microcracks within particles and exposes fresh interfaces, making water molecules, H^+/OH^-, and dissolved oxygen more likely to participate in interfacial corrosion reactions [32]. These interfacial and bulk processes are not isolated but form a closed-loop feedback mechanism through the pathway of "electrolyte decomposition-interfacial evolution-structural degradation-active material loss," ultimately manifesting as lithium loss, active material loss, increased impedance, and gas evolution [33-34].

2.1 Electrolyte Decomposition

In aqueous lithium-ion batteries with LFP, electrolyte decomposition is considered an important contributor leading to capacity fade and reduced lifespan [35]. This mechanism essentially originates from the limited thermodynamic stability window of aqueous systems. Theoretically, the decomposition voltage of water is only 1.23 V, and when the electrode potential exceeds this range, water electrolysis inevitably occurs, resulting in the hydrogen evolution reaction (HER) at the anode and the

oxygen evolution reaction (OER) at the cathode [36-38].

At the anode interface, when the potential falls below the water reduction potential, water molecules are reduced to hydrogen gas and hydroxide ions ($2H_2O + 2e^- \rightarrow H_2 + 2OH^-$). HER dominates the anode-side degradation. It directly consumes electrolyte water, raises local and bulk pH, continuously consumes electrons and reduces Coulombic efficiency. In addition, H_2 evolution disrupts intimate electrode-electrolyte contact, exacerbates interfacial polarization, and accelerates impedance growth [15]. Although HER does not directly corrode the $LiFePO_4$ cathode, the pH elevation it induces may alter the global acid-base environment of the battery, which indirectly shifts the dissolution equilibrium and surface charge properties of the cathode material [18]. At the high-voltage cathode region, water oxidation ($2H_2O \rightarrow O_2 + 4H^+ + 4e^-$) is also inevitable. OER is the dominant side reaction that directly deteriorates the $LiFePO_4$ cathode. H^+ accumulation from OER causes localized acidification at the cathode interface, intensifying chemical corrosion on the LFP/FP surface and promoting Fe, Li and P leaching from the lattice [16;31]. Meanwhile, the generated dissolved oxygen oxidizes leached Fe^{2+} and accelerates the deposition of insulating by-products (e.g., FeOOH, Fe_2O_3) on the cathode surface. O_2 bubble accumulation at the interface also peels off active materials and deteriorates interfacial charge transfer [9;25]. This local acidification and deep penetration of water molecules would damage the LFP surface and hinder internal bulk lithiation processes. As shown in Fig. 2a, the electrochemical stability window of water at different pH values indicates the onset potentials for hydrogen evolution (HER) at low potentials and oxygen evolution (OER) at high potentials [36]. The green dashed lines in the figure indicate how the overpotentials of HER/OER vary with pH, visually illustrating the limitations of the electrochemical window imposed by water decomposition and the influence of local acid-base gradients on side reactions.

The occurrence of HER/OER is also closely related to the solvation structures in the electrolyte (Fig. 2b) [10]. In traditional dilute aqueous electrolytes, Li^+ is primarily coordinated by water molecules, and the system contains a large amount of free water, which is highly reactive at the electrode surface and readily participates in reduction reactions, leading to intense hydrogen evolution. Meanwhile, because anions have difficulty entering the first solvation shell of Li^+, a stable inorganic-rich interfacial protective layer cannot form on the electrode surface, making water decomposition and interfacial side reactions more likely to persist. Fig. 2c illustrates interfacial side reactions on the electrode surface in dilute aqueous electrolytes. Water molecules are reduced at the anode surface to generate H_2 and OH^-, while an incomplete passivation layer forms, exposing active sites and continuously consuming the electrolyte [39]. In contrast, in high-concentration "water-in-salt" electrolytes, the significantly increased salt concentration confines water molecules within limited solvation structures, markedly reducing the amount of free water. At the same time, anions (e.g., $TFSI^-$) enter the Li^+ solvation shell and participate in coordination, forming contact ion pairs or aggregated structures. This solvation restructuring effectively reduces water activity and thermodynamically/kinetically suppresses HER/OER reactions. More importantly, it promotes preferential anion decomposition at the electrode surface, forming a stable, inorganic-rich interfacial film that significantly enhances interfacial stability and expands the electrochemical window.

In summary, electrolyte decomposition in aqueous LFP systems not only directly consumes active material and electrolyte but also, through gas evolution, pH fluctuations, and interfacial instability, induces structural degradation and increased impedance, representing the fundamental bottleneck limiting cycling stability. Understanding this coupled degradation network provides a critical mechanistic basis for developing targeted stabilization strategies.

Nano Research Energy

ISSN 2791-0091 (print); 2790-8119 (online)
https://doi.org/10.26599/NRE.2026.9120266

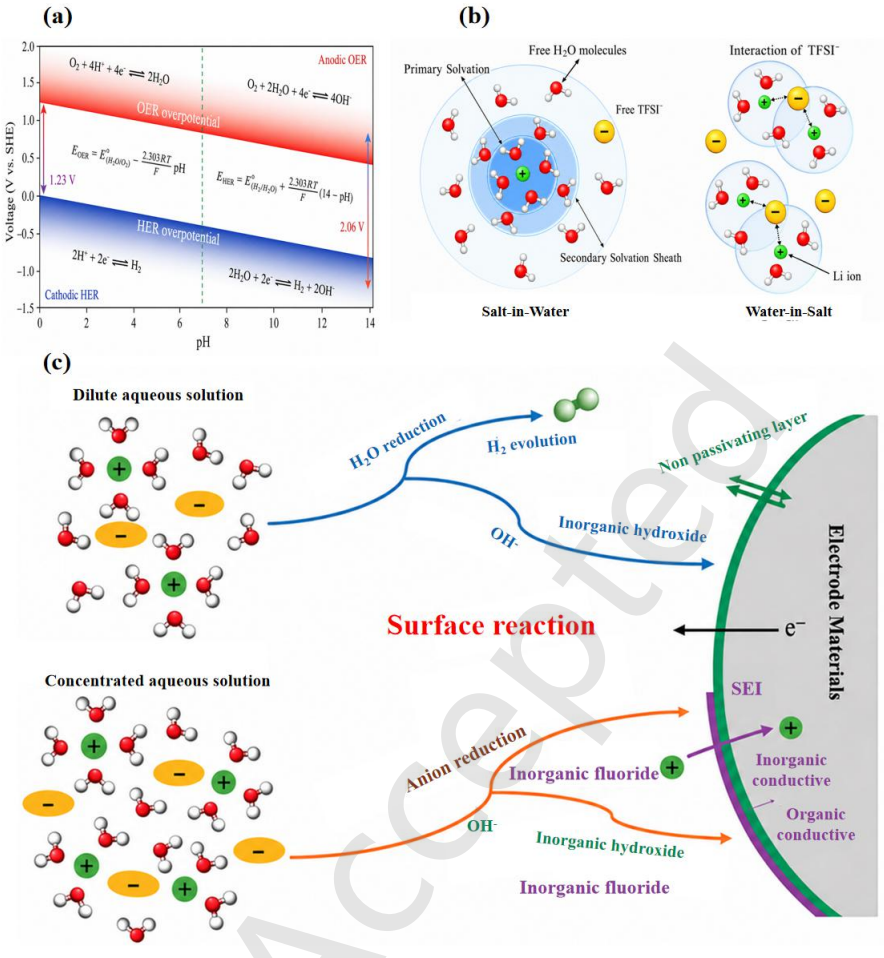

Figure 2 Solvation structures and interfacial behaviors of aqueous electrolytes. (a) Pourbaix diagram of water in aqueous electrolytes at different pH values, showing potential OER/HER processes. Reproduced with permission from Ref. [36], ©The Author(s) 2023. (b) Evolution of Li^+ solvation structures in dilute and water-in-salt electrolytes. Reproduced with permission from Ref. [10], © AAAS. 2015. (c) Illustration of interfacial side reactions on the electrode surface, showing water reduction to H_2 and OH^- and formation of inorganic by-products. Reproduced with permission from Ref. [39], © Wiley-VCH GmbH 2020.

2.2 Material Dissolution and Ion Leaching

In aqueous electrolytes, material dissolution and ion leaching are also considered important causes of capacity decay in LFP. Compared with organic systems, LFP exhibits faster capacity loss in aqueous environments, which is attributed to the chemical and electrochemical instability of the material [40].

Studies have shown that the electrochemical stability of LFP is highly sensitive to the pH of the electrolyte. Under acidic conditions (pH < 5), the proton-rich environment facilitates the dissolution of Fe^{2+} via proton-assisted leaching ($LiFePO_4+3H^+ \rightarrow Li^++Fe^{2+}+H_3PO_4$). This process is thermodynamically favored and accelerates structural collapse, particularly at grain boundaries or defect sites. Concurrently, acidic media suppress HER kinetics at the anode but promote OER and corrosion at the cathode, further enhancing Fe^{2+} oxidation to Fe^{3+} and precipitation of insoluble $Fe(OH)_3$ or $FePO_4$ phases on the electrode surface, which leads to heterogeneous passivation layer and increased impedance [41]. In neutral conditions (pH ≈ 6-8), Fe dissolution is relatively minimized due to the near-equilibrium stability of $LiFePO_4$. However, localized pH shifts caused by OER/HER still induce micro-scale dissolution-reprecipitation cycles. For instance, intermittent OER at the cathode generates H^+, creating transient acidic microdomains that dissolve surface Fe, while adjacent HER zones elevate local OH^-, triggering $Fe(OH)_2/Fe(OH)_3$ formation. Such dynamic fluctuations drive interfacial reconstruction and promote capacity fade over long-term cycling [42-43]. Under strongly alkaline conditions (pH>10), high hydroxide concentration promotes the hydrolysis of P-O bonds on the LFP surface, causing severe leaching of Li and P elements and disrupting the structural integrity of the olivine framework [44]. Dissolved Fe species rapidly form insoluble hydroxides and oxyhydroxides that deposit on the electrode surface, covering electrochemically active sites and aggravating polarization. In addition, dissolved oxygen exhibits stronger oxidizing ability in alkaline media, which further accelerates Fe^{2+} oxidation and surface structural degradation [16]. Researchers also

found that high concentrations of OH^- and dissolved oxygen accelerate cycling decay, further confirming the significant role of chemical corrosion in aqueous systems during degradation [45]. Fluctuations in pH do not simply accelerate chemical corrosion. Rather they significantly alter the ratio of acidic and basic groups on the LFP surface and deteriorate the rheological properties of the electrode slurry, finally causing non-uniform polarization at the microstructural level [46-48].

Regarding specific degradation pathways, Fe^{2+} leaching is one of the most direct sources of active material loss in aqueous LFP electrodes. Fig. 3a illustrates possible particle cracking, loss of electrical contact, and structural disorder in LFP electrodes during cycling. These mechanical defects expose new active sites, allowing water molecules and H^+/OH^- to penetrate the lattice more easily, accelerating Fe^{2+}/Fe^{3+} leaching and interfacial side reactions. Fig. 3b shows the phase composition of LFP particles after cycling, including $FePO_4$ phases, disordered regions, and residual $LiFePO_4$ phases. Part of $LiFePO_4$ is transformed or locally disordered in aqueous environments, leading to active lithium loss and degraded electrochemical performance [49]. Unlike non-aqueous organic electrolytes, where transition metal migration damages the graphite anode SEI, Fe leaching in aqueous systems is primarily governed by water molecule involvement, local pH fluctuations, dissolved oxygen, and oxygen evolution reactions [50-52]. During charging, LFP gradually delithiates to form $FePO_4$ phases, and the Fe^{2+}/Fe^{3+} redox reactions on the electrode surface compete with OER. H^+ accumulation associated with OER causes localized acidification at the cathode interface, exacerbating chemical corrosion on the LFP/FP surface and promoting the leaching of Fe, Li, and P from the lattice surface. The leached Fe^{2+} coordinates with water molecules or anions in the aqueous phase to form hydrated Fe^{2+} complexes, and under oxygen-rich or high-potential conditions, Fe^{2+} may further oxidize to Fe^{3+}. Fig. 3c illustrates Li^+ deintercalation and Fe leaching from the LFP lattice during cycling. Arrows in the figure indicate Fe^{2+}/Fe^{3+} dissolving from the lattice surface into the aqueous phase, potentially forming by-products such as FeOOH or Fe_2O_3. These by-products may redeposit on the surface of LFP particles or within electrode pores, forming an uneven inorganic passivation layer. This deposited layer both covers active sites, reducing the effective area for Li^+ intercalation/deintercalation, and increases interfacial charge transfer resistance, hindering Li^+ transport at the electrode/electrolyte interface, ultimately causing increased polarization and capacity fade.

Besides transition metal leaching, the complex aqueous chemical environment also facilitates the dissolution and intercalation of hetero cations. Zhu et al. [53] found that in salt lake brine systems, Na^+ competes with Li^+ for intercalation and can become trapped in the LFP lattice, resulting in irreversible active lithium loss. It is known that salt lake brine also contains abundant Na^+, Mg^{2+}, and other ions [54-55]. To study the competitive mechanism of impurity ions during electrochemical lithium extraction, cyclic voltammetry (CV) was employed to investigate the reversibility of reactions of different alkali metal ions in LFP electrodes (Fig. 3d) [53]. In different solution systems, the first-cycle CV curves exhibit a distinct oxidation peak at 0.2–0.35 V, corresponding to the initial delithiation of $LiFePO_4$ ($LiFePO_4 \rightarrow FePO_4 + Li^+ + e^-$). During the cathodic scan, reduction peaks are observed only in NaCl and $MgCl_2$ solutions, at approximately 0.34 V and -0.57 V, respectively, indicating that Na^+ and Mg^{2+} can intercalate into the $FePO_4$ lattice. These hetero-cation intercalation events further induce lattice distortion, block one-dimensional Li^+ diffusion channels, and exacerbate irreversible capacity fading during prolonged cycling. Notably, the severity of Na^+/Mg^{2+} competitive intercalation is highly dependent on electrolyte composition, and its contribution to degradation differs drastically between application scenarios. In salt-lake brine and multi-cation electrolyte systems, the concentrations of Na^+ and Mg^{2+} are often comparable to or even higher than that of Li^+, which greatly increases the probability of impurity ions occupying vacant sites in delithiated $FePO_4$ and disrupting subsequent Li^+ (de)intercalation. Under such conditions, hetero-cation competitive intercalation acts as one of the dominant capacity decay mechanisms. In contrast, conventional aqueous lithium-ion batteries are generally configured with high-purity lithium salt electrolytes, such as Li_2SO_4, $LiNO_3$ or LiTFSI, where Na^+ and Mg^{2+} are either absent or present only at trace ppm levels. Accordingly, hetero-cation intercalation is not a universal or dominant degradation pathway in conventional aqueous LFP batteries over short cycling periods. Nevertheless, it can become a non-negligible chronic degradation factor during ultra-long cycling, as trace impurity ions gradually accumulate in the lattice over repeated cycles. This effect becomes more pronounced in mixed-salt, seawater-derived, recycled or low-purity electrolytes, highlighting the importance of controlling and reporting impurity ion concentrations when evaluating the cycling stability of aqueous LFP electrodes.

In summary, material dissolution and ion leaching drive LFP capacity decay in aqueous electrolytes through two interrelated pathways. First, pH fluctuations, dissolved oxygen and OER-induced local acidification promote Fe, Li and P leaching from the lattice, and the subsequent redeposition of insulating by-products reduces electrochemically active sites and increases interfacial charge transfer resistance. Second, competitive intercalation of hetero-cations such as Na^+ and Mg^{2+} triggers lattice distortion and blocks one-dimensional Li^+ diffusion channels, resulting in irreversible active lithium loss. These coupled degradation processes collectively exacerbate cycling fading, and they serve as key targets for the stabilization strategies presented later in this review.

2.3 Lattice Structure Degradation and Phase Transition

Lattice structure degradation and phase transition evolution are another key factor contributing to performance decay in aqueous LFP. Although LFP possesses a stable olivine structure, its charge-discharge process essentially involves a two-phase transition reaction between $LiFePO_4$ and $FePO_4$ [56]. During the transformation from $FePO_4$ to $LiFePO_4$, the system undergo different phase transition pathways, including the ideal homogeneous solid solution mechanism and the more realistic phase boundary migration mechanism (Fig. 3e) [57]. Due to lattice mismatch, the system tends to complete the transformation via phase boundary propagation, during which significant stress concentrations and structural discontinuities occur at the interface [58]. Fig. 3f reveals the defect distribution and energy changes corresponding to Li content evolution along different crystallographic orientations, indicating that the phase transition is not uniform but exhibits pronounced spatial heterogeneity, with local regions prone to defect accumulation and stress concentration [59]. This anisotropic strain accumulates over cycling, ultimately inducing microcracks or even structural fracture within the particles. Compared to non-aqueous systems where nano-structuring or carbon coating could effectively mitigate stress concentration, in aqueous environments, the mechanical stress couples with chemical corrosion by water molecules. On the one hand, water and its decomposition products readily penetrate along defects and phase interfaces, accelerating lattice damage. On the other hand, persistent phase transition stress promotes defect propagation and interfacial instability, significantly accelerating structural degradation [32].

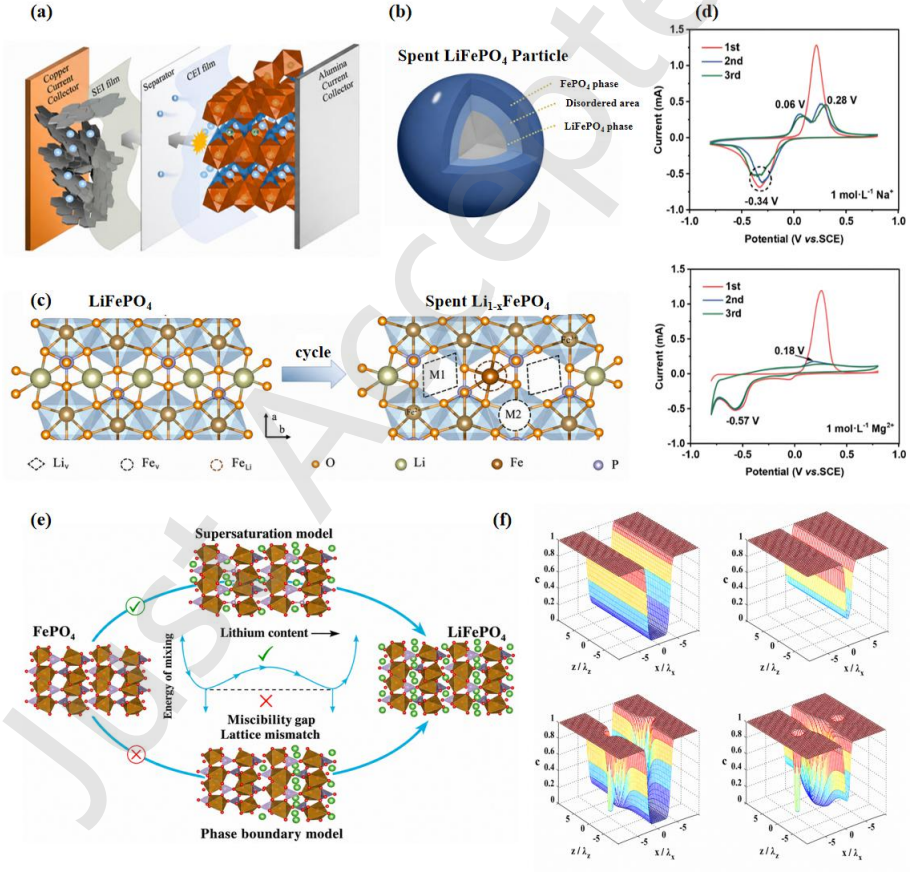

Figure 3 Ion competitive intercalation and surface dissolution-reconstruction mechanisms of LFP/FP electrodes in aqueous environments. (a) Schematic of particle cracking, loss of electrical contact, and structural disorder during cycling. (b) Schematic of phase composition of LFP particles after depletion, including $FePO_4$ phase, disordered regions, and residual $LiFePO_4$ phase. (c) Schematic of Li^+ deintercalation and Fe leaching from the LFP lattice during cycling. Reproduced with permission from Ref. [49], © Wiley-VCH GmbH 2024. (d) CV curves showing competitive intercalation of Na^+/Mg^{2+}. Reproduced with permission from Ref. [53], © Elsevier B.V. 2025. (e) Schematic of solid-solution and phase-boundary models. Reproduced with permission from Ref.[57], © AAAS. 2014. (f) Simulated Li^+ distribution/defect evolution. Reproduced with permission from Ref. [59], © Trans Tech Publications Inc. 2008.

At high-potential delithiation states, the $FePO_4$ phase structure becomes more fragile and more sensitive to the aqueous environment [60]. Zhang et al. [61] found that in aqueous electrolytes, cycled LFP electrodes exhibit formation of iron-containing secondary phases. These secondary phases originate from Fe^{3+} hydrolysis and redeposition in aqueous environments, indicating that $FePO_4$ undergoes partially irreversible transformation at high potentials. The formation of secondary phases not only consumes active material, but also hinders Li^+ diffusion, increases interfacial impedance, and induces further polarization.

In complex aqueous chemical systems (containing Na^+, Mg^{2+}, and other impurity ions), competitive

intercalation of cations alters local lattice charge balance, inducing additional stress concentrations and structural distortions [53;62]. This ion exchange or site-occupancy behavior couples with dissolution-redeposition processes, further amplifying stress accumulation and active material deactivation.

In summary, structural degradation of aqueous LFP is not simply mechanical failure. Rather, cycling stress-induced defect formation further amplifies coupled aqueous interfacial corrosion, elemental leaching, and by-product deposition. Cracks and grain boundary defects increase the contact area and reactive sites between active material and aqueous electrolyte, while dissolved oxygen and side reactions in the aqueous environment exacerbate surface hydrolysis, Fe/P leaching, and local amorphization, ultimately leading to loss of structural integrity and capacity fading.

2.4 Interfacial Side Reactions and Passivation-Layer Evolution

In addition to lattice structure degradation, interfacial side reactions at the LFP electrode surface are also important contributors to performance decay. Cracks, grain boundary defects, and freshly exposed surfaces induced by lattice degradation increase the likelihood of interfacial reactions between LFP/FP and aqueous electrolytes, thereby exacerbating deposition of surface by-products and the unstable evolution of passivation layers. Next, we discuss in detail how these side reactions occur at the electrode surface.

At the cathode interface, oxygen evolution reaction, transition metal dissolution and anion decomposition occur simultaneously, representing key factors limiting cycling stability. At high operating potentials, OER-derived gas accumulates at the electrode surface, inducing microcracks in the passivation layer and exposing fresh active material to the electrolyte, which causes continuous electrochemical degradation [63]. The adsorption and rearrangement of interfacial water molecules, regulated by surface active sites and ionic environment, further modulate water oxidation kinetics and the intensity of side reactions [64]. At anodic potential, OER products react with dissolved Fe ions to form a mixed passivation layer. This amorphous or poorly crystalline structure increases interfacial resistance and reduces Coulombic efficiency [65]. Importantly, the passivation layer is not a static film. The initial solid layer provides temporary protection, but repeated potential cycling and persistent water penetration drive continuous breakdown and reformation, sustaining long-term interfacial instability [66]. Heterocations such as Na^+ and Mg^{2+} further complicate interfacial chemistry. These impurity ions participate in interfacial reactions, act as local catalysts or form non-ideal layered phases, which aggravate interfacial hysteresis and accelerate degradation [67].

In summary, the interfacial layer in aqueous LFP systems is not a passive reaction product but a continuously evolving chemical system. Its composition, thickness and stability evolve with cycling, jointly governing ion transport and polarization behavior. Clarifying these dynamic interfacial mechanisms provides a critical basis for developing targeted stabilization strategies.

2.5 Coupling Mechanisms of Multiple Degradation Processes

The aforementioned degradation pathways do not operate independently. Instead, they interact synergistically through positive feedback loops, collectively accelerating structural deterioration and capacity fade of aqueous LFP electrodes. Three dominant coupling mechanisms govern the overall degradation process.

First, lattice hydration and transition metal dissolution form a self-amplifying cyclic coupling. Water molecules penetrating the olivine lattice weaken Fe-O bonding in FeO_6 octahedra and reduce the activation energy for Fe^{2+}/Fe^{3+} leaching, exacerbating transition metal dissolution. The dissolved iron species further catalyze interfacial water decomposition and promote the formation of loose, porous iron-based passivation layers, which fail to block further water infiltration into the bulk lattice. This failure loop of water penetration, Fe dissolution and passivation layer continuously expands the active degradation interface and accelerates bulk structural degradation of the active material.

Second, impurity-cation intercalation couples with interfacial side reactions and structural degradation. Trapped Na^+/Mg^{2+} induce permanent lattice distortion and generate abundant structural defects at particle surfaces and grain boundaries. These defect sites act as preferential reactive sites for Fe dissolution and water decomposition, accelerating the growth of heterogeneous and cracked passivation layers. In turn, the defective passivation layer cannot effectively screen hetero-cations, increasing the probability of impurity ion intercalation and further aggravating lattice channel blockage. This mutual promotion between lattice structural damage and interfacial deterioration accounts for the rapid capacity fade observed in multi-cation brine systems.

Third, proton intercalation couples with lattice hydration and local acidification. Protons inserted into the olivine framework react with lattice oxygen to form hydroxyl groups, causing localized acidification inside particles that further promotes Fe leaching and surface structural amorphization. Meanwhile, proton-induced lattice contraction generates microcracks in particle bulks, which provide additional diffusion channels for water penetration and intensify lattice hydration. The synergistic effect of proton insertion and water uptake jointly accelerates the collapse of the olivine crystal framework during long-term cycling.

Clarifying these coupled degradation loops provides a theoretical basis for targeted decoupling strategies. For instance, constructing a dense and ion-selective interfacial

layer can simultaneously block water penetration, suppress impurity cation intercalation, and reduce transition metal dissolution, thereby breaking the positive feedback of multiple degradation processes.

2.6 Experimental Discrimination of Intercalation and Hydration

Experimentally, proton intercalation, hydration, and impurity-cation intercalation could be distinguished via combined electrochemical characterization, elemental quantification, structural diffraction, and spectroscopic fingerprinting [68-69].

Electrochemical tests could serve as a rapid non-destructive pre-screening approach. Cyclic voltammetry directly identifies impurity-cation intercalation. Na^+ and Mg^{2+} insertion generates distinct extra redox peaks at potentials separate from the intrinsic $LiFePO_4/FePO_4$ couple [53]. In contrast, proton intercalation manifests as a broad, highly polarized redox tail below the main lithium intercalation plateau. Lattice hydration produces no additional faradaic peaks, only elevated parasitic background currents from accelerated water decomposition. Electrochemical quartz crystal microbalance (EQCM) further differentiates them by mass response. Hydration induces continuous large mass gain from trapped water molecules in the lattice. Impurity-cation insertion produces stepwise mass increments proportional to the molar mass of trapped hetero-ions, and proton intercalation causes negligible net mass change due to the extremely low mass of H^+ [15].

Ex-situ elemental and thermal analysis enable quantitative differentiation of the three processes. Inductively coupled plasma optical emission spectrometry (ICP-OES) performed on fully washed cycled electrodes directly quantifies lattice-trapped Na^+ and Mg^{2+}. Concentrations significantly higher than the pristine baseline confirm the occurrence of impurity-cation intercalation. Thermogravimetric analysis (TGA) coupled with solid-state ^1H nuclear magnetic resonance (NMR) distinguishes hydration from proton intercalation. Lattice hydration shows prominent mass loss at 100-250 °C, which corresponds to the release of crystalline water. Proton intercalation exhibits minimal low-temperature mass loss but features characteristic sharp proton peaks in NMR spectra, corresponding to the formation of protonated $HFePO_4$ phases [19].

Moreover, structural diffraction and spectroscopic techniques provide direct structural evidence at the atomic scale. In-situ or ex-situ X-ray diffraction (XRD) differentiates the three processes by their distinct lattice evolution behaviors. Hydration induces uniform and fully reversible lattice expansion that recovers completely after high-temperature dehydration. Proton intercalation leads to reversible unit-cell contraction along the *b*-axis accompanied by characteristic $HFePO_4$ secondary phase diffraction peaks. Impurity-cation intercalation causes permanent, irreversible peak shifts, due to trapped hetero-ions blocking the one-dimensional diffusion channels [70]. Complementary X-ray photoelectron spectroscopy (XPS) depth profiling and Fourier-transform infrared spectroscopy (FTIR) further verify the distribution and chemical state of the relevant species. Hydration shows strong O-H vibrational bands and surface-enriched hydroxyl groups. Proton intercalation features distorted P-O-H bonding signals, and impurity-cation intercalation presents uniform Na/Mg elemental distribution across particle cross-sections, which distinguishes lattice incorporation from surface precipitate contaminants.

This multi-technique combinatorial approach enables both qualitative identification and quantitative evaluation of the three degradation processes, providing a standardized analytical workflow for mechanistic studies of aqueous $LiFePO_4$ batteries.

3 Stabilization Strategies for Aqueous LFP Batteries

The preceding sections have systematically elaborated the multi-dimensional degradation mechanisms of LFP in aqueous electrolytes, including electrolyte decomposition, transition metal dissolution, lattice structural degradation and interfacial side reactions. These coupled failure pathways can be mitigated through targeted stabilization strategies covering intrinsic material regulation, interface engineering and electrolyte system optimization [69;71]. Fig. 4 summarizes the core modification approaches and their synergistic effects. Elemental doping enhances the thermodynamic stability of the crystal lattice. Surface coating suppresses aqueous chemical corrosion and improves electronic conductivity, and morphological regulation optimizes mechanical stability and ion diffusion kinetics particularly under high-rate cycling. Meanwhile, electrolyte optimization and cathode prelithiation fundamentally reduce active lithium loss and widen the electrochemical stability window to ensure long-term durability [72]. The following sections discuss each strategy and its corresponding stabilization mechanism in detail.

Nano Research Energy
ISSN 2791-0091 (print); 2790-8119 (online)
https://doi.org/10.26599/NRE.2026.9120266

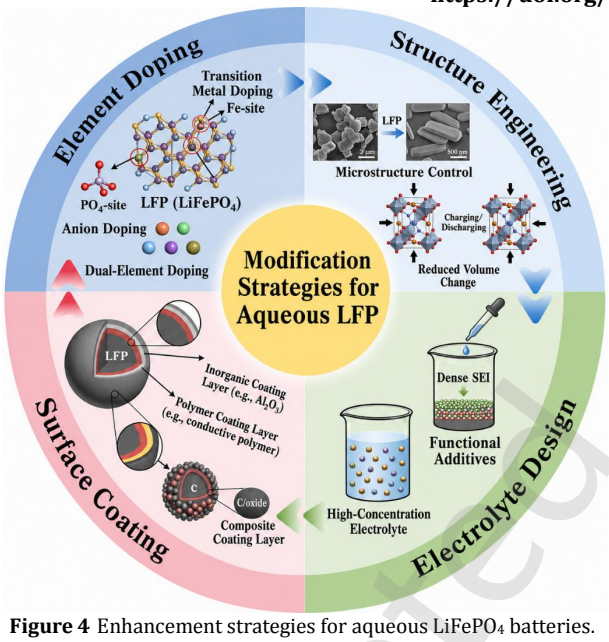

Figure 4 Enhancement strategies for aqueous $LiFePO_4$ batteries.

3.1 Elemental Doping

As previously discussed, capacity decay of aqueous $LiFePO_4$ is primarily associated with Fe leaching, lattice distortion, phase transition stress, and water-induced interfacial side reactions. Elemental doping can regulate the local coordination environment, defect chemistry, and electronic structure of $LiFePO_4$ [73]. By enhancing intrinsic electronic conductivity and Li^+ diffusion kinetics [74], doping serves as an important material-design strategy for mitigating bulk structural degradation.

It should be noted that most studies on LFP doping modifications are based on non-aqueous lithium-ion batteries or half-cell tests, primarily demonstrating the effects of doping on intrinsic conductivity, Li^+ diffusion barriers and lattice parameters [75], which cannot be directly equated with corrosion resistance or Fe leaching suppression in aqueous electrolytes [76]. Therefore, in this work, elemental doping is regarded as an indirect strategy for bulk stabilization and transport kinetics optimization, and its actual contribution to the stability of aqueous LFP requires further validation through cycling performance, Fe/P/Li leaching, interfacial by-products, and impedance evolution in aqueous electrolytes.

3.1.1 Li-Site Doping

Introducing small-radius metal ions (e.g., Zr, Cr, Nb, Mg, Na, Ti, Al) into Li sites is a widely adopted strategy to address the low intrinsic electronic conductivity and sluggish Li^+ diffusion of $LiFePO_4$ [77]. Its performance enhancement relies on two core pathways: improved electronic conductivity and accelerated Li^+ transport.

The incorporation of multivalent or high-valence dopants generates cationic defects and raises the concentration of mixed Fe^{2+}/Fe^{3+} valence states, converting the intrinsic semiconductor into a p-type semiconductor. Chung et al. [74] found that this effect boosts the electronic conductivity of $LiFePO_4$ by approximately 8 orders of magnitude to 10^{-2} S cm^{-1}. Dopants with distinct electronegativity and valence also tune the Fe^{2+}/Fe^{3+} redox energy level and shift the delithiation potential (Fig. 5a), enabling voltage optimization [78]. Besides, moderate Li-site doping induces mild lattice distortion, creates additional Li vacancies, and widens the one-dimensional diffusion channels along the [010] direction. Local structural regulation lowers the migration barrier and optimizes transport kinetics within the olivine framework of PO_4 tetrahedra and FeO_6 octahedra (Fig. 5b) [79]. Electrochemically, optimized doping reduces charge-transfer resistance and alleviates polarization (Fig. 5c) [80]. These benefits arise from the synergistic regulation of defect chemistry, local structure and transport kinetics, rather than a mere conductivity [81-82].

Nevertheless, the one-dimensional diffusion feature imposes strict constraints on dopant site and concentration. Kinetics improvement only occurs when foreign ions stably occupy lattice sites and maintain [010] channel continuity. Dopants segregated at grain boundaries, surfaces or interstitial sites tend to block diffusion pathways and aggravate local polarization, which remains a long-standing debate in doping engineering [83-84].

Notably, most Li-site doping studies are performed in non-aqueous systems and focus on electronic/ionic transport and rate capability. Whether this strategy can suppress Fe/P leaching and water-induced interfacial side reactions in aqueous LFP still requires dedicated validation via aqueous cycling tests and dissolution characterization. Overall, lattice-substituted Li-site doping delivers net benefits but demands precise process control. Future work should leverage first-principles calculations to pre-screen dopant species, occupancy and optimal doping levels, and combine systematic structural characterization to avoid channel blockage.

3.1.2 Fe-Site Doping

Introducing metal ions (e.g., Mg, Mo, Co, V, Mn, Ni, Zn) at Fe sites in LFP is an important strategy for tuning the local structure and electrochemical properties [85-86]. Unlike Li-site doping, which mainly modulates Li^+ vacancies and diffusion channels [87], Fe-site doping directly affects the FeO_6 octahedra and Fe^{2+}/Fe^{3+} redox centers [88], thereby influencing the local coordination environment, Li/Fe antisite defects, continuity of Li^+ diffusion channels, and delithiation potential. Substitution of Fe by transition metals M forms a TM-LFP structure, altering the local FeO_6 octahedral environment and surrounding electronic structure (Fig. 5d) [78], providing a structural basis for subsequent defect control, lattice distortion, and transport optimization. Appropriate Fe-site doping can maintain continuity of one-dimensional Li^+ diffusion channels by weakening local Li-O interactions, adjusting lattice volume, and suppressing Li/Fe antisite defects.

Fe-site doping exerts a dual effect on Li^+ transport (Fig. 5e) [89]. When dopants stably occupy Fe sites and induce moderate lattice adjustment, diffusion channels remain open and unobstructed. In contrast, unstable occupancy, excessive local distortion, or elevated antisite defect density may cause crossed diffusion pathways, channel blockage, or partial Li^+ trapping. Hence, the core of Fe-site doping lies in precise control of dopant occupancy, concentration, and impact on channel continuity.

Representative dopants deliver distinct functions based on their valence state, ionic radius, and electronic effects. Goonetilleke et al. [90] confirm that Mg^{2+} preferentially and stably occupies Fe sites, suppressing antisite defects while inducing favorable lattice distortion to improve performance without hindering Li^+ deintercalation. Multivalent dopants such as Mo and V introduce adequate Li^+ vacancies while maintaining olivine stability, with V doping notably enhancing rate performance [91-92]. Co-doping with Ni and Mn optimizes the local coordination and reduces charge-transfer resistance, while trace Ti or Mn doping accelerates reaction kinetics and introduces additional redox activity to boost capacity and operating voltage [93-94]. Fundamentally, these improvements stem from the synergistic regulation of FeO_6 coordination and Li^+ channel optimization.

Fe-site doping is highly sensitive to dopant concentration, and excessive doping inevitably causes adverse effects. Unstable occupancy, high formation energy could not only fail to optimize diffusion channels but also induce channel blockage, local structural distortion, and additional antisite defects. For instance, elevated Mn doping triggers severe Jahn–Teller distortion from high-spin Mn^{3+}, twisting the cathode framework and generating new Li-Fe antisite defects that impede Li^+ diffusion and charge transfer [95]. Moreover, dissolution of transition metal ions such as Mn^{2+} during cycling destabilizes the cathode structure and accelerates capacity fade, with limited improvement at low temperatures [96].

For aqueous LFP systems, the evaluation of Fe-site doping must be extended to aqueous chemical stability. The reduced impedance and accelerated Li^+ diffusion reflect optimized bulk and interfacial transport kinetics (Fig. 5f), but do not directly confirm improved corrosion resistance in aqueous electrolytes [96]. Meanwhile, parameters such as bandgap, formation energy, elastic properties, and delithiation voltage must be compatible with the aqueous electrolyte stability window. Excessively elevated operating potential may trigger the leaching of dopant metals under local acidification, dissolved oxygen, and OER by-products may introduce new active material loss. Therefore, the actual stabilizing effect of Fe-site doping in aqueous LFP requires further validation via ICP leaching analysis, post-cycling XPS/TEM characterization, and long-term aqueous cycling tests.

In summary, Fe-site doping combines structural stabilization and kinetic optimization potential but exhibits an obvious dual-sided effect. Moderate isovalent Mg^{2+} doping suppresses antisite defects and stabilizes the Fe-site lattice, and multivalent dopants such as V^{5+} enhance electronic and ionic transport via defect chemistry regulation. Excessive doping or unstable occupancy causes lattice distortion, Li^+ channel blockage, and even metal dissolution. For aqueous LFP, Fe-site doping serves as an auxiliary strategy for bulk structural stabilization and transport kinetics optimization, while its practical efficacy needs to be evaluated in synergy with surface coating and electrolyte regulation.

3.1.3 Anion Doping

Besides cation doping, anion substitution at O or P sites serves as another key strategy to tailor the electronic structure, local coordination and Li^+ diffusion kinetics of $LiFePO_4$ [97-99]. Unlike Li/Fe-site cation doping that modulates cation sublattices, anion doping directly perturbs PO_4 tetrahedra and adjacent Li-O bonding, tuning Li^+ migration by altering O-site charge distribution and modifying lattice parameters [100-102]. As depicted in Fig. 5g [103], O-site substitution with Cl^-, F^- and S^{2-} reshapes the local coordination framework, providing a structural basis for reduced Li^+ migration barriers and optimized diffusion pathways.

Halogen doping at O sites delivers the most notable improvement in Li^+ transport. Wang et al. [103] found that the Li^+ migration barrier of pristine $LiFePO_4$ is ~0.572 eV, which decreases to 0.209 eV and 0.283 eV for Cl^- and F^- doped samples, respectively. Cl doping achieves the largest barrier reduction by widening Li^+ diffusion channels via local lattice expansion from its larger ionic radius, whereas F doping mainly regulates the PO_4 framework electron cloud through its high electronegativity. For larger S^{2-} anions, O-site substitution induces moderate lattice expansion and modulates the spatial environment around Li^+ channels, lowering the migration barrier to 0.488 eV (Fig. 5h). Beyond bulk O-site substitution, N

doping functions as a surface-specific regulation strategy targeting the $LiFePO_4$ (010) active facets. As illustrated in Fig. 6a, N doping reconstructs surface Li^+ migration pathways and local Li-O/N coordination, optimizing Li-Li distances and diffusion channels along specific directions. This allows N doping to modulate the electronic structure, reduce Li^+ cross-interface migration resistance, yielding synergistically enhanced electronic and ionic conductivity [104].

For P-site doping (e.g., boron), moderate addition refines particle size, mitigates agglomeration and improves charge transport, but is constrained by a strict concentration threshold. Excessive B doping may induce oxygen vacancies and local structural disorder, leading to active lithium loss and degraded electrochemical performance. Hence, P-site doping should prioritize low dosage, controlled site occupancy and defect suppression rather than pursuing high doping levels [105-106].

3.1.4 Summary of Elemental Doping Strategies

Overall, current evidence for anion doping is largely derived from structural models and migration barrier calculations, demonstrating improved Li^+ transport kinetics via O-site coordination tuning, PO_4 electronic structure modification and (010) surface diffusion optimization. For aqueous $LiFePO_4$, such bulk and surface kinetic optimization theoretically alleviates polarization and local stress, yet does not directly confirm suppression of water-induced corrosion, Fe/P leaching or OER-related interfacial side reactions. Therefore, anion doping should be regarded as an auxiliary strategy for electronic structure and Li^+ transport regulation, and its aqueous stabilization effect still requires validation via long-term cycling tests, ICP leaching analysis, post-cycling XPS/TEM characterization and EIS monitoring. Table 1 summarizes the significant effects of elemental doping on $LiFePO_4$ performance, which provides researchers with a systematic guide for selecting dopant elements and processes, aiding in further optimization of battery design.

Nano Research Energy

ISSN 2791-0091 (print); 2790-8119 (online)
https://doi.org/10.26599/NRE.2026.9120266

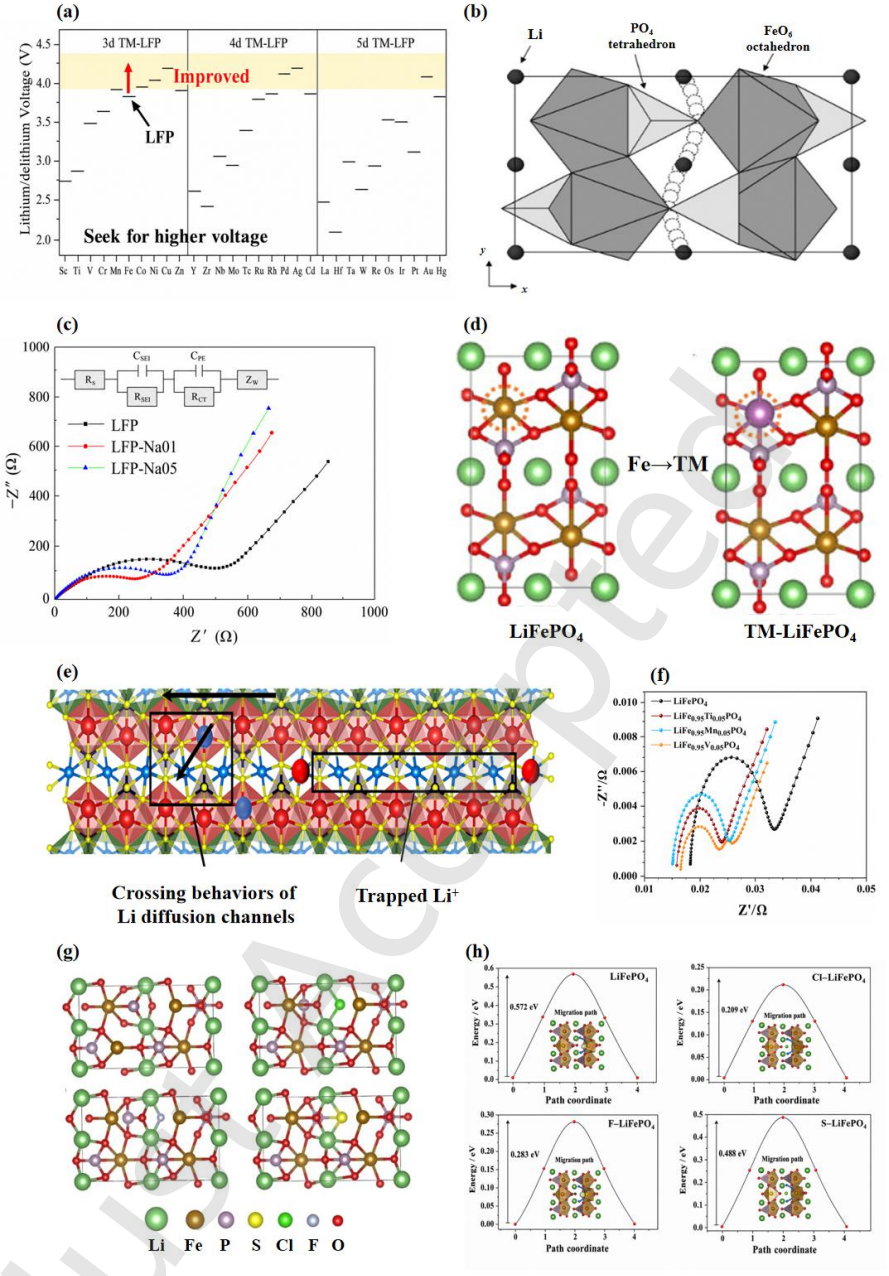

Figure 5 Regulatory mechanisms of doping on $LiFePO_4$ crystal structure (a) Effects of various 3d, 4d, and 5d transition metal dopants on $LiFePO_4$ delithiation voltage. Reproduced with permission from Ref. [78], © OAE Publishing Inc. 2022. (b) Schematic of olivine $LiFePO_4$ crystal structure, showing PO_4 tetrahedra, FeO_6 octahedra, and Li^+ one-dimensional diffusion channels. Reproduced with permission from Ref. [79], © American Chemical Society 2005. (c) EIS of $LiFePO_4$ with varying Na doping levels. Reproduced with permission from Ref. [80], © Elsevier B.V. 2021. (d) Schematic of structural evolution of TM-LFP formed by substitution of Fe with transition metals. Reproduced with permission from Ref. [78], © OAE Publishing Inc. 2022. (e) Schematic illustrating the impact of Fe-site doping on continuity of Li^+ one-dimensional diffusion channels. Reproduced with permission from Ref. [89], © Elsevier B.V. 2025. (f) EIS analysis of typical Fe-site doped samples. Reproduced with permission from Ref. [96], © Springer Berlin Heidelberg 2024.(g) Crystal structure models of pristine $LiFePO_4$, Cl-doped, F-doped, and S-doped $LiFePO_4$. (h) Comparison of Li^+ migration barriers in pristine, Cl-, F-, and S-doped $LiFePO_4$. Reproduced with permission from Ref. [103]. © Wiley-VCH GmbH 2024.

Table 1 Overview of the Electrochemical Performance of Elementally Doped $LiFePO_4$ in non-aqueous electrolytes

Dopant Element	Doping Site	Optimal Doping Amount	Electrochemical Performance (Initial Capacity and Cycling Performance)
Na [80]	Li	$Li_{0.99}Na_{0.01}FePO_4$	80.9 mAh g^{-1}, 86.7% (10 C,500 cycles)
Nb [81]	Li	$Li_{0.95}Nb_{0.01}FePO_4$	96.7 mAh g^{-1}, 96% (10 C,200 cycles)
Mo [91]	Fe	$LiFe_{0.98}Mo_{0.02}PO_4$	141.5 mAh g^{-1}, 98% (0.1 C, 100 cycles)
V [92]	Fe (or P)	$LiFe_{0.95}V_{0.05}PO_4$	119 mAh g^{-1}, 98% (1500 mA g^{-1}, 100 cycles)
Mn [93]	Fe	$LiFe_{0.77}Mn_{0.23}PO_4$	80.9 mAh g^{-1}, 84% (1 C,100 cycles)
Ti [94]	Fe	$LiFe_{0.98}Ti_{0.02}PO_4$	160 mAh g^{-1}, 98% (0.2 C, 50 cycles)

F [101]	O	$LiFePO_{3.85}F_{0.15}$	115.7 mAh g^{-1}, 92.8% (30 C, 50 cycles)
S [107]	O	$LiFePO_{3.78}S_{0.22}$	112.7 mAh g^{-1}, 98% (0.2 C, 50 cycles)
Cl [108]	O	$LiFePO_{3.98}Cl_{0.02}$	105.3 mAh g^{-1}, 91.5% (10 C, 500 cycles)

3.2 Surface Coating

The degradation of aqueous $LiFePO_4$ systems mainly originates from interfacial instability, including corrosion induced by water molecules, continuous electrolyte decomposition, and dynamic rupture of interfacial layers. Therefore, the core goal of surface coating is to construct an artificial interfacial layer that suppresses side reactions while ensuring efficient Li^+ transport. Unlike in nonaqueous systems, where coatings primarily enhance conductivity, in aqueous environments the primary role of the coating layer is to serve as a chemically stable barrier that prevents direct contact between water molecules and the active material. Simultaneously, this interfacial layer must possess good ionic conductivity and mechanical stability to accommodate volume changes during cycling [109].

3.2.1 Carbon Coating

Carbon coating is the most fundamental and cost-effective strategy owing to its wide availability and excellent electronic conductivity. In-situ carbon coating during high-temperature synthesis acts as a reducing agent to prevent Fe^{2+} oxidation, suppresses particle agglomeration, and constructs an inter-particle electronic conductive network [110-112]. For process optimization, studies show that sucrose-derived amorphous carbon with a precisely controlled mass fraction of ~9% (heat-treated at 600 °C) forms a continuous conductive network and serves as a physical barrier, reducing direct contact between the aqueous electrolyte and the LFP surface [113-114]. Advanced hot-pressed carbon fiber coating further improves electrode mechanical toughness, preserving coating integrity and preventing interfacial delamination [115]. As shown in Fig. 6b, scanning electron microscopy (SEM) and energy dispersive spectroscopy (EDS) mapping confirm that the carbon layer forms a continuous or semi-continuous conductive film on LFP particles, improves inter-particle contact and lowers electronic transport resistance [116]. Overall, carbon coating primarily functions as electronic conductive network construction and interfacial contact improvement, rather than complete isolation from aqueous corrosion.

Heteroatom doping (e.g., N, F) further increases conductive active sites in the carbon layer and shortens the Li^+ diffusion path. Wang et al. [117] synthesized N-doped carbon-coated composites using polybenzoxazine, which delivered an initial discharge capacity of 150 mAh g^{-1} at 2 C with 98.2% capacity retention after 150 cycles. With an F-doped carbon 3D conductive network, $LiFePO_4$ maintained 95.4% of its initial capacity after 1000 cycles at 10 C [118].

Novel highly conductive carbon materials, represented by graphene and carbon nanotubes, further push the rate performance limit. As illustrated in Fig. 6c, a graphite intercalation-assisted strategy embeds $FeCl_3$ between graphite layers, and forms a $LiFePO_4$/graphite composite via solvothermal reaction and annealing [119]. The graphite framework provides long-range electron transport pathways and uniformly disperses LFP particles, enabling 107 mAh g^{-1} at an ultra-high rate of 60 C and 95% capacity retention after 2000 cycles. Wang et al. [120] reported N-doped graphene-coated thin LFP nanosheets with exposed (010) active facets (Brunauer-Emmett-Teller (BET) surface area of 199.3 m^2 g^{-1}), which retained 78 mAh g^{-1} at 100 C.

Constructing a multi-dimensional dual-carbon synergistic conductive network is another effective approach to optimize kinetics under extreme conditions [121]. Wu et al. [122] combined amorphous carbon with graphitized carbon nanotubes, and the dual-carbon coated composite maintained 59% capacity after 100 cycles at an extreme rate of 120 C. Fan et al. [123] prepared porous nano-$LiFePO_4$@C microspheres, which exhibited an excellent low-temperature discharge capacity of 117 mAh g^{-1} at −20 °C. These results demonstrate the great potential of multi-dimensional carbon composites and heteroatom doping in boosting the overall electrochemical performance of LFP.

Table 2 summarizes different carbon coating approaches, comparing carbon sources, coating methods, key preparation features and corresponding electrochemical performance. Notably, most of the high-rate and low-temperature performance data are obtained from non-aqueous lithium-ion battery systems, which mainly verify the enhancement of electronic conduction and reaction kinetics. Its corrosion resistance in aqueous LFP still requires validation via Fe/P/Li leaching measurements, post-cycling XPS/TEM characterization and impedance evolution analysis.

In summary, carbon coating plays a critical role in improving conductivity and mitigating water-induced corrosion, thus enhancing the rate capability and cycling stability of aqueous LFP batteries. However, it has limitations in accelerating Li^+ diffusion and enhancing structural stability, which cannot fully address the chemical stress and interfacial degradation induced by aqueous electrolyte decomposition. Single carbon coating is therefore insufficient to overcome all degradation pathways, and integration with inorganic compound coatings and ion-conductive coatings is necessary to achieve synergistic performance enhancement, as discussed in the following sections.

Nano Research Energy
ISSN 2791-0091 (print); 2790-8119 (online)
https://doi.org/10.26599/NRE.2026.9120266

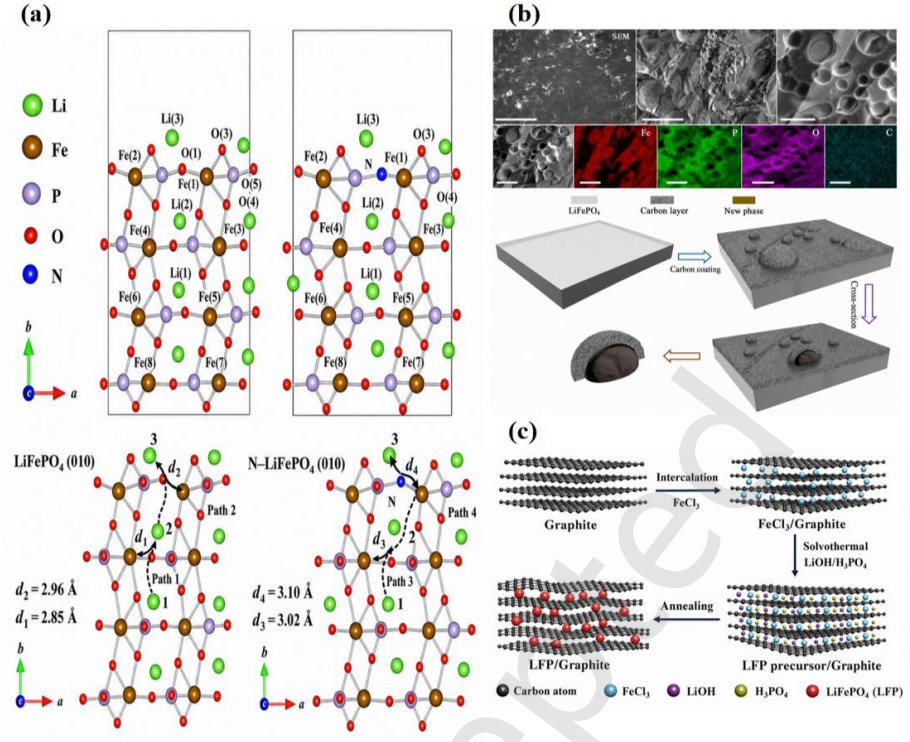

Figure 6 Regulatory mechanisms of N doping and carbon coating on $LiFePO_4$. (a) Structural models and surface Li^+ migration pathways of pristine $LiFePO_4$ (010) and N-doped $LiFePO_4$ (010). Reproduced with permission from Ref. [104], © Elsevier B.V. 2015. (b) Microstructure, elemental distribution, and coating process of carbon-coated $LiFePO_4$. Reproduced with permission from Ref. [116], © Springer Nature 2018. (c) Schematic of graphite intercalation-assisted preparation of $LiFePO_4$/graphite composite Reproduced with permission from Ref. [119], © American Chemical Society 2021.

Table 2 Comparison of Structural Features and Electrochemical Performance of $LiFePO_4$ Coated with Various Carbon Sources

Carbon Source	Coating Method	Initial/ Rate	Cycling Performance
Polybenzoxazine [117]	N-Doped Carbon Coating	150 mAh g^{-1} at 2 C	98.2%, 150 cycles, 2 C
Graphene [124]	Graphene coating	70 mAh g^{-1} at 60 C	85%, 1000 cycles, 10 C
Graphene [120]	N-Doped Graphene Aerogel Coating	78 mAh g^{-1} at 100 C	89%,1000 cycles, 10 C
Carbon Nanotubes [122]	Amorphous Carbon + CNT Dual-Carbon	120 mAh g^{-1} 0.1 C, -25°C	59%, 100 cycles, 120 C
Porous Carbon Microspheres [123]	Porous Nano $LiFePO_4$@C Microspheres	117 mAh g^{-1}, 1 C, –20 °C	——

3.2.2 Inorganic Compound Coating

In addition to carbon coating, introducing inorganic compounds with good chemical stability and low cost (e.g., SnO_2 [125], MoO_2 [126], WO_2 [127], and TiN) for surface modification is another key strategy to enhance the electronic conductivity, tap density, and structural stability of $LiFePO_4$. Such coating layers can stabilize the interface without compromising the olivine-type $LiFePO_4$ framework, and greatly enhance ion and electron transport kinetics [65]. Liu et al. [126] found that co-coating with 5 wt% MoO_2 and carbon increased the apparent Li^+ diffusion coefficient by an order of magnitude compared to the unmodified sample, reaching 1.0×10^{-10} cm^2 s^{-1}. Highly conductive inorganic coatings also exhibit significant capacity enhancement potential. Zhang et al [128] reported that coating with 10% nano-TiN allowed the material to achieve 159 mAh g^{-1} at 0.1 C, and 40 mAh g^{-1} at 5 C high rate.

In aqueous batteries, the focus is on corrosion resistance. Inorganic protective layers such as AlF_3 act as stable surface barriers, reducing direct contact between LFP and aqueous electrolytes. Studies have shown that constructing a 1 wt% AlF_3 coating on LFP particles via chemical precipitation improves cycling stability in 1 M Li_2SO_4 aqueous electrolyte, with 100-cycle capacity retention increasing from ~82% to over 93%. This indicates that the key role of inorganic coatings in aqueous systems is not HF resistance, but to suppress surface side reactions induced by water molecules/H^+, Fe dissolution, and inorganic by-product deposition [43]. Fig. 7a-7b further illustrate the dual role of AlF_3 inorganic coatings in aqueous $LiFePO_4$ [65]. Fig. 7a shows that bare $LiFePO_4$ particles suffer from limited electronic conduction and Li^+ diffusion due to insufficient interfacial contact or surface insulating layer formation, whereas uniform AlF_3 coating improves inter-particle contact and reduces transport resistance. Fig. 7b shows that the AlF_3 coating isolates the LFP surface from direct contact with water molecules,

H^+/OH^-, and dissolved oxygen, thereby mitigating surface corrosion and side reactions. Thus, it is evident that the primary role of inorganic compound coatings in aqueous systems is not the HF corrosion resistance, which is commonly emphasized in non-aqueous systems, but rather the suppression of water-induced surface hydrolysis, Fe/P leaching, and inorganic by-product deposition.

3.2.3 Ion-Conductive Coating

Traditional carbon or metal oxide coatings primarily enhance the electronic conductivity of $LiFePO_4$ and inter-particle conductive networks. However, charge compensation during cycling relies on both electron transport and rapid Li^+ migration across the particle surface, coating layer and electrolyte. A coating that only improves electronic conduction without continuous Li^+ transport pathways still restricts interfacial ion transport, raising charge-transfer resistance and degrading rate performance. Therefore, ion-conductive coatings are recognized as a critical strategy to simultaneously optimize interfacial stability and Li^+ cross-interface migration.

Among fast ion conductors, $Li_3V_2(PO_4)_3$ with an open 3D framework is the most widely used. Zhong et al. [129] constructed a composite that improved electronic conductivity by 3 orders and Li^+ diffusion coefficient by 1 order, delivering 131.3 mAh g^{-1} at 10 C with 95.1% capacity retention after 200 cycles. Liang et al. [130] synthesized porous nanosheet composites that reached 161.5 mAh g^{-1} at 0.1 C, approaching the theoretical capacity. Besides $Li_3V_2(PO_4)_3$, nano-Li_3PO_4 and perovskite-type materials also deliver favorable modification effects. Zhao et al. [131] applied a hybrid coating of amorphous carbon and dispersed nano-Li_3PO_4, boosting the initial capacity by 30 mAh g^{-1} at 5 C relative to the pristine sample. Shu et al. [132] fabricated a dual-layer coating of carbon and $La_{0.56}Li_{0.33}TiO_3$, which synergistically constructed electron- and ion-conductive layers to enhance transport kinetics and interfacial stability, achieving 98.3% capacity retention after 100 cycles at 5 C and 62.3 mAh g^{-1} at 30 C. It should be noted that these dual-layer coating studies were mostly conducted in non-aqueous $LiPF_6$ electrolytes. The reported HF corrosion resistance cannot be directly extrapolated to water corrosion resistance in aqueous electrolytes.

For aqueous LFP systems, the functional focus of ion-conductive coatings should shift from HF corrosion resistance to blocking aqueous electrolyte corrosion while maintaining selective Li^+ transport. In recent years, sodium super ionic conductor (NASICON)-type materials such as lithium aluminum titanium phosphate (LATP) have been widely adopted as artificial interphases to build Li^+ selective transport barriers. In a 2 M Li_2SO_4 aqueous electrolyte, LATP-coated LFP retained over 85% capacity after 500 cycles, compared with less than 50% for the uncoated sample, and ICP measurements showed that Fe leaching was reduced by approximately one order of magnitude [133]. Amorphous $LiTi_2(PO_4)_3$ coatings have also been proven to effectively suppress electrode-electrolyte side reactions and form robust protective interphases for high-voltage aqueous systems. Meanwhile, innovative spray deposition techniques enable low-cost, scalable fabrication of thick, uniform protective layers on LFP.

Therefore, the core function of ion-conductive coatings in aqueous LFP is not merely to improve rate performance, but to construct an artificial interface at the electrode/aqueous electrolyte interface that provides both chemical barriers and a Li^+ selective transport layer. As shown in Fig. 7c, while a single carbon coating can improve electronic conductivity, the absence of continuous Li^+ transport channels may still result in restricted Li^+ migration and increased interfacial polarization [134]. In contrast, ion-conductor/carbon composite coatings provide both an electron transport network and Li^+ cross-interface migration pathways, alleviating mismatches between electron and ion transport rates. For aqueous LFP, such composite coatings should additionally block direct contact of H_2O, H^+/OH^-, dissolved oxygen, and OER by-products with the LFP/FP surface, thereby suppressing Fe leaching, surface hydrolysis, and inorganic by-product deposition.

3.2.4 Summary of Surface Coating Strategies

As summarized in Fig. 7d, the three main coating strategies have distinct functional priorities. Carbon coating is mature and low-cost, capable of constructing long-range electronic conductive networks and reducing polarization, but it cannot fully block water molecules and OER/HER by-products from corroding the LFP surface. Inorganic compound coatings offer favorable chemical stability and mechanical rigidity to reduce direct contact between the aqueous electrolyte and active material, but their intrinsic electronic conductivity is inferior to carbon, and excessively thick or discontinuous coatings may raise Li^+ diffusion resistance. Ion-conductive coatings enable selective Li^+ transport across the interface but usually require combination with carbon materials to compensate for insufficient electronic conduction. In summary, each single coating strategy has inherent limitations, so future surface engineering of aqueous LFP should move beyond single conductive or protective layers, and toward multifunctional artificial interfaces integrating an electron conductive layer, water-corrosion-resistant layer and selective Li^+ transport layer. Only by simultaneously suppressing water corrosion, Fe/P leaching and interfacial by-product deposition while maintaining fast cross-interface Li^+ migration can the long-term cycling stability of aqueous LFP be truly improved.

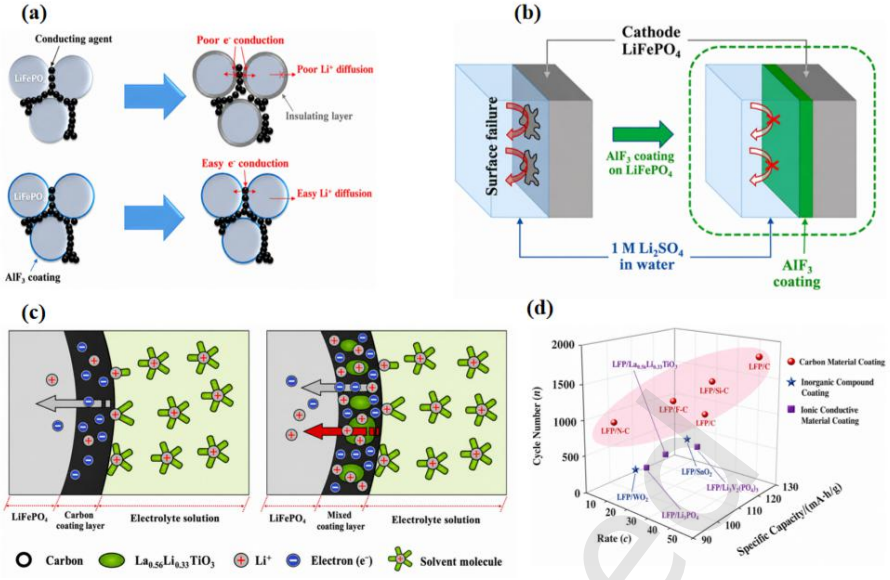

Figure 7 Surface coating modification strategies of $LiFePO_4$ and their interfacial protection mechanisms in aqueous electrolytes. (a) Illustration of AlF_3 coating improving inter-particle electron/ion transport and interfacial contact in $LiFePO_4$. (b) Illustration of the protective mechanism of AlF_3 coating in 1 M $LiFePO_4$ aqueous electrolyte. Reproduced with permission from Ref. [65], © American Chemical Society 2017. (c) Illustration of interfacial transport differences between carbon coating and ion-conductor/carbon composite coating. Reproduced with permission from Ref.[134], © Elsevier Ltd. 2015. (d) Comprehensive comparison of different surface modification strategies in terms of rate performance, specific capacity, and cycle life.

3.3 Morphology and Structural Regulation

Surface coatings effectively block water-induced corrosion and improve interfacial conductivity, but their effects are confined to particle surfaces. Since the anisotropic volumetric strain during LFP phase transition originates from the bulk, interface modification alone cannot fundamentally suppress the initiation of particle microcracks. Accordingly, morphology and structural regulation serve as key strategies for alleviating mechanical stress and enhancing structural stability.

Simple nano-structuring shortens Li^+ and electron transport paths, reduces polarization and improves rate performance, but excessive size reduction elevates the risk of interfacial side reactions [135]. Delacourt et al. [136] synthesized ~140 nm LFP with a discharge capacity of 147 mAh g^{-1} at 5 C. In aqueous systems, 80 nm LFP also reduces charge-transfer resistance by approximately 30%. Nevertheless, when particle size drops below 50 nm, the enlarged specific surface area increases electrolyte contact, significantly accelerating water adsorption and Fe leaching. Therefore, structural design has evolved from mere size reduction to balancing diffusion paths, interfacial reaction area and stress distribution.

To balance kinetic enhancement and interfacial side reaction suppression, facet engineering and multilevel structure design have become core directions for morphology optimization, mainly including (010) facet orientation, hollow structures, three-dimensional oriented porous structures, and hierarchical assembly [137]. At the facet level, the surface energy and Fe exposure density of different crystal planes directly govern water adsorption and side reaction rates [138]. $LiFePO_4$ enriched with low-surface-energy (010) facets maintains stable Li^+ diffusion channels and reduces exposure of highly reactive Fe sites, thus mitigating surface hydrolysis and Fe leaching in aqueous environments[62;139]. At the particle structure level, three representative architectures deliver distinct optimization effects. First, hollow structures buffer the volumetric strain induced by the $LiFePO_4/FePO_4$ two-phase transition via internal cavities. Hollow $LiFePO_4$ features distinct internal cavities, which provide space for stress release during cycling and shorten Li^+ diffusion paths within particles (Fig. 8a) [140]. Corresponding rate performance and cycling results (Fig. 8b-c) indicate that hollow structures maintain high capacity output and stable capacity retention across different rates, demonstrating that rational cavity design supports both kinetic performance and structural stability [141]. Second, three-dimensional oriented porous structures with interconnected channels improve electrolyte infiltration and reduce Li^+ diffusion resistance (Fig. 8d–f) [142]. Compared with conventional LFP, this architecture achieves higher capacity, better rate recovery and superior long-term cycling stability by alleviating electrode polarization. Third, oriented nanosheets and hierarchical structures optimize Li^+ transport directions through facet-oriented exposure and ordered assembly [141-143]. As shown in Fig. 8g [144], $LiFePO_4$ undergoes nucleation, growth, oriented aggregation, further stacking, and peeling/curving to form hierarchically structured architectures with orientation features. Such structures favor exposure of active facets related to Li^+ migration and shorten diffusion distances along specific crystallographic directions, thereby enhancing rate performance while mitigating local stress concentration.

Overall, morphology and structural regulation play important roles in alleviating stress concentration, suppressing particle cracking, and controlling water molecule penetration. However, compared to elemental doping and surface coating, structural regulation

primarily affects mechanical and transport aspects and has limited ability to suppress interfacial chemical reactions and electrolyte decomposition. In addition, excessive nano-structuring or highly porous structures may instead exacerbate interfacial side reactions. Therefore, structural regulation alone cannot comprehensively address degradation in aqueous systems and must be synergistically designed with interface engineering and electrolyte optimization. Moreover, particle-level morphology regulation must be coordinated with electrode-scale ion transport, particularly under practically relevant active-material loadings [145]. Future research should focus on integrated stress regulation and interface protection, for example, combining hollow or hierarchical structures with stable coatings to achieve synergistic enhancement of mechanical and chemical stability.

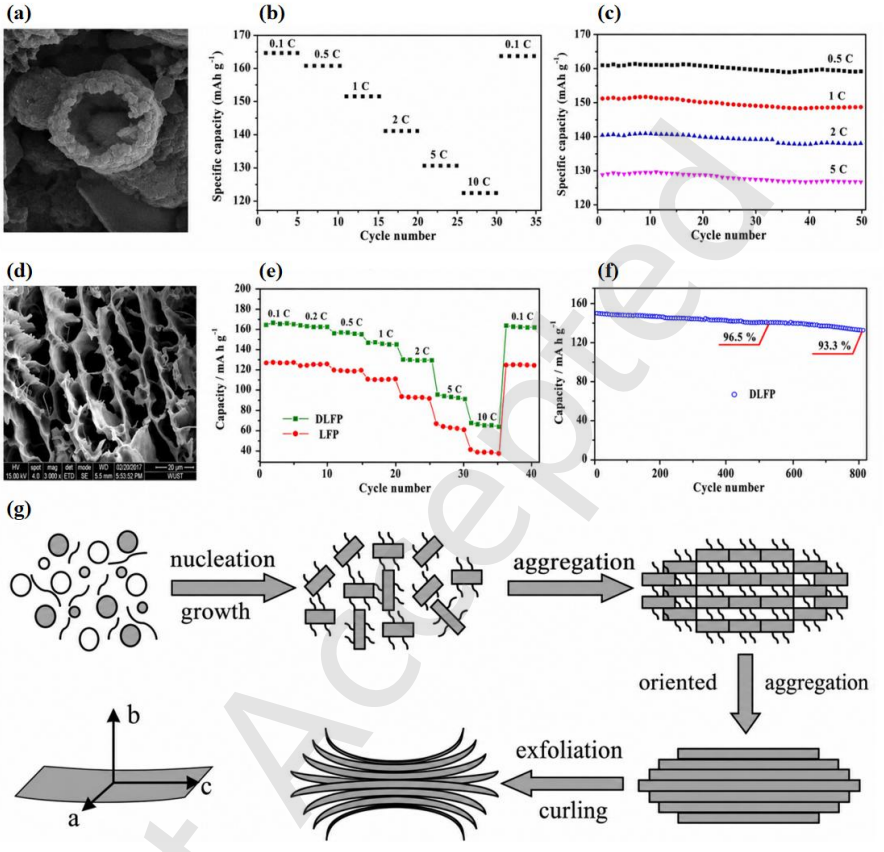

Figure 8 Effects of $LiFePO_4$ morphology and structural regulation on Li^+ diffusion pathways, rate performance, and cycling stability. (a) SEM image of hollow-structured $LiFePO_4$. Reproduced with permission from Ref.[140], © Elsevier Ltd. 2021 (b) Rate performance of hollow-structured $LiFePO_4$ at different rates. (c) Cycling stability of hollow-structured $LiFePO_4$ at different rates. Reproduced with permission from Ref. [141], © Elsevier Ltd. 2015. (d) SEM image of three-dimensional oriented porous $LiFePO_4$. (e) Comparison of rate performance between three-dimensional oriented porous $LiFePO_4$ and conventional $LiFePO_4$. (f) Long-term cycling performance of three-dimensional oriented porous $LiFePO_4$. Reproduced with permission from Ref. [142], © Elsevier B.V. 2018. (g) Schematic of the formation mechanism of oriented nanosheet/hierarchical $LiFePO_4$ structures Reproduced with permission from Ref. [144], © The Author(s) 2013.

3.4 Cathode Lithium Supplementation and Electrolyte Optimization

The long-term stable operation of aqueous LFP batteries is mainly constrained by two factors: (1) the intrinsically narrow thermodynamic stability window of aqueous electrolytes, which easily triggers OER at high potential and HER at low potential, causing gas evolution, pH fluctuations, Fe dissolution, and interfacial side reactions; (2) irreversible loss of active lithium during the first and long-term cycles, leading to capacity fade and reduced Coulombic efficiency. Therefore, electrolyte optimization should serve as a core strategy for stabilizing aqueous LFP, aiming to reduce free water activity, regulate Li^+ solvation structure, expand the electrochemical stability window, and suppress HER/OER. In contrast, cathode lithium supplementation is primarily used to compensate for initial active lithium loss. Although this concept can be adopted from non-aqueous lithium-ion batteries, its chemical compatibility and side reaction risks in aqueous systems still require further validation.

Cathode prelithiation through the incorporation of lithium-rich sacrificial additives into the cathode slurry has been widely investigated as an effective strategy to compensate for the initial irreversible capacity loss in non-aqueous lithium-ion batteries. These additives are generally oxidized during the first charge, thereby releasing additional Li^+ to offset active lithium consumption at the anode. For example, Diaz-Lopez et al. [146] reported Li_2O:$Li_{2/3}Mn_{1/3}O_{5/6}$ nanocomposites as cathode prelithiation additives, which increased the first-cycle charge capacity of $LiFePO_4$ to 165 mAh g^{-1} with only 2 wt% additive. Similarly, N-Co/N-Li_2O nanocomposites can form Li_2O/metal composite

structures through Li diffusion during thermal treatment, providing extra lithium during the subsequent electrochemical activation process (Fig. 9a) [147]. In addition, LiF/Co composite lithium supplements can be prepared through the reaction between CoF_3 and molten Li, in which metallic Co improves the electronic conductivity while LiF serves as the lithium-containing phase with lithium-supplementing capability (Fig. 9b) [148].

It should be noted that most of these cathode prelithiation additives were originally designed for non-aqueous lithium-ion batteries. Their primary purpose is to compensate for initial active-lithium loss rather than to suppress water decomposition or stabilize electrode/electrolyte interfaces in aqueous systems. Therefore, when these additives are considered for aqueous $LiFePO_4$-based batteries, several additional factors must be carefully evaluated, including their chemical stability in water, compatibility with electrolytes, oxidation potential relative to the $LiFePO_4$ operating window, and possible side effects.

Compared with directly transferring water-sensitive sacrificial additives from non-aqueous batteries, a more relevant approach in aqueous lithium-ion batteries is in-situ electrochemical lithiation/activation of water-stable insertion-type anodes using a lithiated cathode as the Li^+ reservoir. A representative example is the aqueous $LiFePO_4$//$LiTi_2(PO_4)_3$ full-cell configuration, in which $LiFePO_4$ provides cyclable Li^+ and NASICON-type $LiTi_2(PO_4)_3$ serves as a low-potential anode capable of reversible Li^+ insertion/extraction [149]. Sun et al. [150] further demonstrated that nanoparticulate $LiTi_2(PO_4)_3$/C could function as a stable anode in aqueous rechargeable lithium batteries when paired with $LiFePO_4$ in Li_2SO_4-based electrolyte. In such systems, the initial charging process electrochemically activates the $LiTi_2(PO_4)_3$-based anode without using Li, stabilized Li powder and highly reactive sacrificial lithium compounds. This strategy is particularly suitable for aqueous batteries because both $LiFePO_4$ and $LiTi_2(PO_4)_3$ are phosphate-based insertion compounds with relatively high structural stability in near-neutral aqueous media, and the lithiation process can be controlled within the electrochemical stability window of the electrolyte to minimize parasitic OER/HER reactions. Another aqueous-compatible strategy is to employ lithium-excess cathodes as internal Li^+ reservoirs. For instance, flexible aqueous Li-ion batteries based on $Li_{1.1}Mn_2O_4$ cathodes and carbon-coated $LiTi_2(PO_4)_3$ anodes have shown that a lithium-rich cathode can supply sufficient Li^+ for reversible operation of the anode in aqueous electrolytes [151]. Although this strategy is not a conventional approach, it offers a practical route for compensating lithium deficiency and enabling stable full-cell operation under aqueous conditions.

Nevertheless, increasing the active lithium source via prelithiation alone is insufficient to maintain long-term stability in aqueous systems. Optimizing the electrolyte to reduce free water activity, regulate Li^+ solvation structure and suppress HER/OER is more critical to mitigate water decomposition, pH fluctuations and interfacial side reactions. The most representative strategy is the "water-in-salt" (WIS) super concentrated electrolyte. Suo et al. [10] developed a 21 mol kg^{-1} WIS electrolyte, which expanded the electrochemical stability window from 1.23 V to 3.0 V by drastically reducing free water activity and restructuring Li^+ solvation shells, demonstrating the great potential of high-concentration salt strategies for high-voltage aqueous batteries. To further overcome the solubility limits of a single high-concentration salt and minimize free water activity, researchers introduced asymmetric quaternary ammonium salts (e.g., $Me_3EtNTFSI$) to construct mixed WIS electrolytes. The addition of these asymmetric ions effectively disrupts the crystallization equilibrium of the original salt solution, raising the total salt concentration unprecedentedly to 63 M, greatly expanding the thermodynamic operational limits of the aqueous system [152-153].

In terms of solvation structure regulation, introducing hydrogen-bond acceptors such as dimethyl sulfoxide (DMSO) can strongly interact with water molecules, restructure the hydrogen-bond network in the electrolyte, and reduce the proportion of free water. As shown in Fig. 9c, when the electrolyte structure shifts from a high free-water state to a DMSO-coordinated associated solvation structure, the reduction activity of water molecules at the electrode surface decreases, and HER is suppressed. Fig. 9d further illustrates that the introduction of DMSO alters interactions among cations, anions, water molecules, and hydrogen-bond acceptors, preventing abundant high-activity free water molecules near the interface. Fig. 9e visually compares the high free-water content in low-DMSO systems with the "no free water" state in higher DMSO content systems. Thus, the key mechanism by which DMSO suppresses HER is not merely diluting water molecules, but enhancing water stability via hydrogen-bond acceptor interactions and solvation structure reconstruction, thereby delaying HER and mitigating interfacial side reactions induced by pH fluctuations [154].

In addition, functional co-solvents or interfacial additives can promote the formation of inorganic-rich protective layers on the electrode surface, reducing direct contact between water molecules and active materials and mitigating continuous capacity fade and impedance growth caused by side reactions. Moreover, by introducing antifreeze co-solvents such as ethylene glycol, their hydrogen-bond interactions with water molecules reduce free water activity and suppress water decomposition, thereby improving ion transport and cycling stability of LFP aqueous batteries under low-temperature conditions [155].

Overall, cathode lithium supplementation compensates for active lithium loss during initial and early cycles via oxidative decomposition of sacrificial additives, improving initial Coulombic efficiency and reversible capacity, yet it cannot fundamentally mitigate sustained capacity decay caused by water decomposition and interfacial side reactions. Additionally, their water stability and side reaction risks in aqueous environments require further systematic

validation. In contrast, electrolyte optimization acts as the core strategy for long-term cycling stability. By reducing free water activity, reconstructing hydrogen-bond networks and regulating Li^+ solvation structures, it directly suppresses HER/OER and the associated pH fluctuations. Nevertheless, electrolyte optimization alone cannot address phase transition stress and particle cracking. Therefore, future work should integrate electrolyte engineering with doping, surface coating and structural regulation to construct a multi-strategy synergistic system covering active lithium compensation, free water suppression, artificial interface stabilization and structural stress buffering.

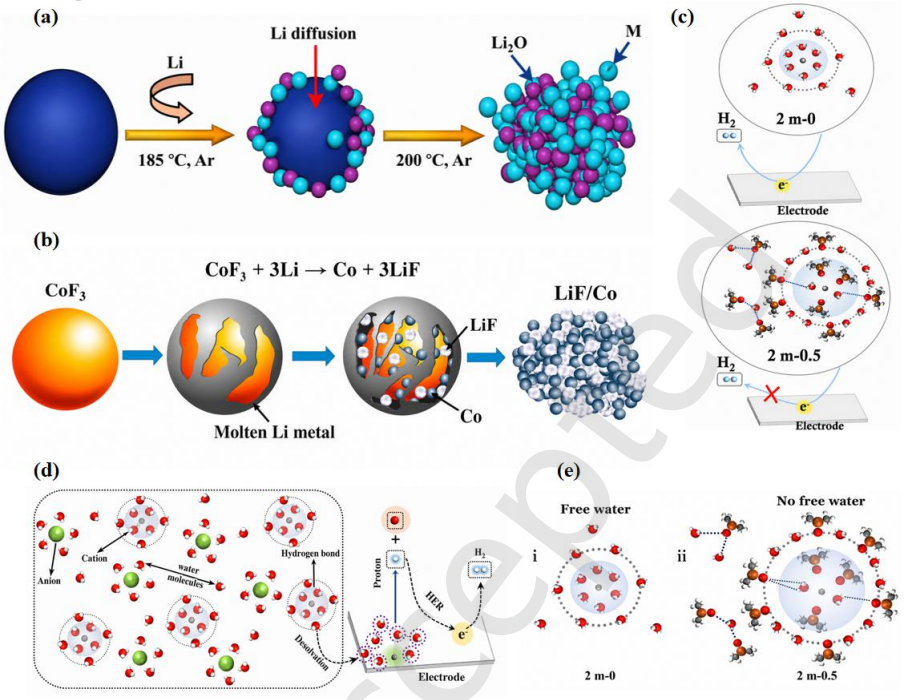

Figure 9 Mechanistic illustration of cathode lithium supplementation and electrolyte structure regulation on the stability of aqueous $LiFePO_4$. (a) Schematic of the formation process of N-Co/N-Li_2O nanocomposite lithium supplement. Reproduced with permission from Ref. [147], © Springer Nature 2016. (b) Preparation mechanism of LiF/Co nanocomposite lithium supplement. Reproduced with permission from Ref. [148], © American Chemical Society 2016. (c) Schematic of water molecule solvation states and HER behavior in different electrolyte structures. (d) Schematic of interactions among cations, anions, water molecules, and hydrogen-bond acceptors in the electrolyte. (e) High free-water content in low-concentration systems. Reproduced with permission from Ref. [154], © American Chemical Society 2021.

4 Conclusions and Perspectives

4.1 Conclusions

This work systematically analyzes the coupled degradation mechanisms of $LiFePO_4$ in aqueous batteries and the corresponding modification strategies, establishing a multi-dimensional synergistic optimization framework.

The capacity decay of aqueous LFP stems from a multi-factor coupled failure process driven by both thermodynamic limitations and kinetic evolution, rather than a single degradation pathway. At high charging potentials, the Fe^{2+}/Fe^{3+} redox competes with the oxygen evolution reaction, lowering charge utilization and inducing Fe dissolution. Meanwhile, anisotropic volumetric strain during repeated Li^+ (de)intercalation triggers particle microcracks, which provide channels for deep penetration of water and its decomposition products. This forms a vicious feedback loop of phase transition stress, defect evolution and chemical corrosion, ultimately causing lattice disorder and irreversible active material loss. Fig. 10 presents a summarizing framework for this study.

To address these issues, stabilization strategies have evolved from single-factor empirical modification to multi-scale collaborative design. Elemental doping can improve lattice stability and may reduce the susceptibility of LFP to Fe dissolution by regulating the local coordination environment and defect chemistry. Surface coating and morphological regulation buffer phase transition stress and construct artificial barriers to suppress water corrosion. By reducing free-water activity and promoting anion-involved solvation structures/interphase formation, highly concentrated electrolytes could expand the electrochemical stability window. Cathode lithium supplementation could compensate for initial active lithium loss. The synergistic combination of these approaches enables comprehensive performance enhancement of aqueous LFP systems.

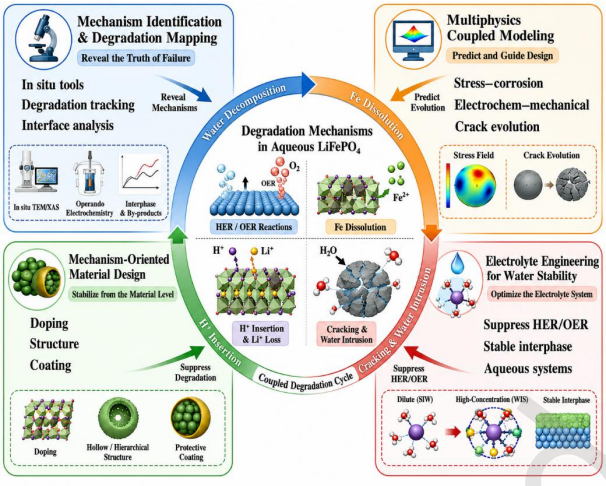

Figure 10 Summary diagram of research on aqueous LFP batteries.

4.2 Perspectives

With high industrial maturity and low manufacturing costs in non-aqueous systems, LFP holds great promise for large-scale aqueous battery applications. Future research should go beyond laboratory performance optimization and focus on the balanced development of cost, safety and cycling life for practical deployment. Key research directions are proposed as follows.

First, develop low-cost electrolyte systems for grid energy storage. Current water-in-salt electrolytes effectively widen the electrochemical window but suffer from exorbitant cost, severely restricting their large-scale application. Future work should prioritize low-cost alternatives with high-salt effects or novel interfacial film-forming additives to regulate the solvation structure, achieving wide voltage window and long cycle life under low salt concentrations. Taking advantage of the moderate operating potential of LFP, precise control of polarization and interfacial environment can largely avoid OER even in weakly acidic dilute electrolytes, providing inherent feasibility for ultra-low-cost grid-scale energy storage.

Second, extend LFP applications to electrochemical lithium extraction from salt lake brines. Benefiting from its excellent Li^+ selective intercalation property, LFP exhibits strategic value in lithium recovery from complex brine systems. The research focus has shifted from concept verification to the synergy of high selectivity, long service life and scalable production. Future studies should develop facet engineering, defect-targeted doping and molecular-sieving anti-corrosion coatings, coupled with flow reactor design and in-situ electrode regeneration, to build high-selectivity, long-life LFP-based electrodes for industrial brine lithium extraction.

Third, strengthen multi-physics simulation and engineering technology development. For complex practical service conditions, more efforts should be devoted to multi-physics coupled modeling combined with advanced thick-electrode coating processes, to reveal the dynamic microstructural evolution of LFP under high salinity and multivalent ion corrosion, including electrochemical stress, lattice volume variation and interfacial phase transition.

Fourth, establish standardized evaluation criteria under practically relevant conditions. Many aqueous LFP studies are currently conducted using low active-material loadings and excessive electrolyte, which may overestimate electrode-level capacity and cycling stability while obscuring limitations at the practical cell level. Future studies should therefore report active-material loading (mg cm^{-2}), areal capacity (mAh cm^{-2}), and the electrolyte-to-capacity ratio (mL Ah^{-1} or g Ah^{-1}), in addition to conventional gravimetric capacity. Long-term Coulombic efficiency, energy efficiency, and cycle life based on a clearly defined end-of-life criterion should also be evaluated under realistic charge-discharge rates and temperature conditions. Moreover, the energy density of a full battery should be calculated by considering electrodes, electrolyte, separator, current collectors, and other inactive components, rather than using the mass of the cathode active material alone. Establishing these standardized evaluation criteria will enable meaningful comparison among different aqueous LFP systems and facilitate their transition from laboratory demonstrations to grid-scale energy-storage applications.

In general, stability research on aqueous LFP has transitioned from empirical modification to mechanism-driven design based on synergistic thermodynamic and kinetic regulation. Multi-scale matching of material structure, electrolyte solvation and interfacial chemistry is the core to realizing stable long-cycle operation of aqueous LFP, which also provides a general framework for interfacial stability research of other aqueous cathode materials.

Acknowledgements

The authors acknowledge financial support from the the National Natural Science Foundation of China (22408239).

Declaration of conflicting interests

The authors declare no conflicting interests regarding the content of this article.

Data availability

All data needed to support the conclusions in the paper are presented in the manuscript and/or the Supplementary Materials. Additional data related to this paper may be requested from the corresponding author upon request.

References

[1] von Wald Cresce, A., K. Xu. Aqueous lithium-ion batteries. *Carbon Energy* **2021**, *3*, 721-751.

[2] Yamada, Y.; K. Usui; K. Sodeyama; S. Ko; Y. Tateyama, A. Yamada. Hydrate-melt electrolytes for high-energy-density aqueous batteries. *Nat. Energy* **2016**, *1*, 16129.

[3] Armand, M., J.M. Tarascon. Building better batteries. *Nature* **2008**, *451*, 652-657.

[4] Chao, D., S.-Z. Qiao. Toward High-Voltage Aqueous Batteries: Super- or Low-Concentrated Electrolyte? *Joule* **2020**, *4*, 1846-1851.

[5] Gulavani, V.; B. John; P. Sharma, A. Yengantiwar. Water-Based Wonders: Exploring Recent Progress in Aqueous Lithium-Ion Batteries. *Energy Fuels* **2025**, *39*, 15525-15553.

[6] Guo, X.; H. He; S. Zhao; H. Dong; P.R. Shearing; R. Jervis, J. Lin. Unveiling aqueous lithium-ion batteries via advanced modelling and characterisation: A review. *Energy Stor. Mater.* **2024**, *70*, 103505.

[7] Yang, Q.; N. Jiang; X. Li; C. Zhi, J. Qiu. Electrochemical engineering in aqueous metal-ion batteries. *Science Bulletin* **2025**, *70*, 2157-2172.

[8] He, P.; J.-L. Liu; W.-J. Cui; J.-Y. Luo, Y.-Y. Xia. Investigation on capacity fading of $LiFePO_4$ in aqueous electrolyte. *Electrochim. Acta* **2011**, *56*, 2351-2357.

[9] Wang, Z.-R.; Y.-L. Zhang; R.-Z. Zhang; W.-W. Li; J. Song, S.-L. Liu. The Road Ahead for Aqueous Lithium-ion Batteries. *cMat* **2025**, *2*, e70010.

[10] Suo, L.; O. Borodin; T. Gao; M. Olguin; J. Ho; X. Fan; C. Luo; C. Wang, K. Xu. "Water-in-salt" electrolyte enables high-voltage aqueous lithium-ion chemistries. *Science* **2015**, *350*, 938-943.

[11] Borodin, O.; L. Suo; M. Gobet; X. Ren; F. Wang; A. Faraone; J. Peng; M. Olguin; M. Schroeder; M. Ding; E. Gobrogge; A.v.W. Cresce; S. Munoz; J. Dura; S. Greenbaum; C. Wang, K. Xu. Liquid Structure with Nano-Heterogeneity Promotes Cationic Transport in Concentrated Electrolytes. *ACS Nano* **2017**, *11*, 10462-10471.

[12] Lukatskaya, M.R.; J.I. Feldblyum; D.G. Mackanic; F. Lissel; D.L. Michels; Y. Cui, Z. Bao. Concentrated mixed cation acetate "water-in-salt" solutions as green and low-cost high voltage electrolytes for aqueous batteries. *Energy Environ. Sci.* **2018**, *11*, 2876-2883.

[13] Zhang, L. Unveiling Gas Evolution in Sustainable Aqueous Batteries by Online Electrochemical Mass Spectrometry: Progress and Perspectives. *ACS Mater Au* **2025**, *5*, 896-905.

[14] Hu, J.; H. Guo; Y. Li; H. Wang; Z. Wang; W. Huang; L. Yang; H. Chen; Y. Lin, F. Pan. Understanding Li-ion thermodynamic and kinetic behaviors in concentrated electrolyte for the development of aqueous lithium-ion batteries. *Nano Energy* **2021**, *89*, 106413.

[15] Zhang, L.; C. Zhang, E.J. Berg. Mastering Proton Activities in Aqueous Batteries. *Adv. Mater.* **2025**, *37*, 2407852.

[16] Luo, J.-Y.; W.-J. Cui; P. He, Y.-Y. Xia. Raising the cycling stability of aqueous lithium-ion batteries by eliminating oxygen in the electrolyte. *Nat. Chem.* **2010**, *2*, 760-765.

[17] Yin, Y.; Y.-h. Wen; Y.-l. Lu; J. Cheng; G.-p. Cao, Y.-s. Yang. Electrochemical Performance and Capacity Fading Mechanism of $LiFePO_4$ at Different pH Aqueous Electrolyte Solutions. *Chin. J. Chem. Phys.* **2015**, *28*, 315-322.

[18] Zhang, Y.; A. Hu; D. Hou; G. Kwon; D. Xia; L. Li, F. Lin. A Comparative Study of Degradation Behaviors of $LiFePO_4$, $LiMn_2O_4$, and $LiNi_{0.8}Mn_{0.1}Co_{0.1}O_2$ in Different Aqueous Electrolytes. *J. Electrochem. Soc.* **2024**, *171*, 020526.

[19] Zhang, L.; F. Kühling; A.-M. Mattsson; L. Knijff; X. Hou; G. Ek; T. Dufils; F. Holm Gjørup; I. Kantor; C. Zhang; W.R. Brant; K. Edström, E.J. Berg. Reversible Hydration Enabling High-Rate Aqueous Li-Ion Batteries. *ACS Energy Lett.* **2024**, *9*, 959-966.

[20] Kakarla, A.K.; Z. Akhtar; J. Kim; M. Yoon; D. Lee, J. Choi. Beyond the Limits of Lithium Iron Phosphate: Cutting-Edge Innovations Toward High Performance and Sustainability for Next-Generation Batteries. *Interdiscip. Mater.* **2025**, *4*, 812-849.

[21] Fu, L.; X. Wang; R. Zhang; R. Li; G. Wei, M. Li. Proton co-intercalation enabled high-performance aqueous multivalent metal-ion batteries. *J. Mater. Chem. A* **2025**, *13*, 24300-24319.

[22] Luo, F.; W. Lai; L. Chen; S. Yang; Z. Huang; X. Chen; F. Xiao; Q. Qian; Q. Chen, L. Zeng. Toward Sustainable Spent Cathode Recycling Technology: Failure Mechanism, Advancing Technology and Prospect. *Rare Metals* **2026**, *45*, e70303.

[23] Zhang, Y.; X. Wang; L. Huang; C. Bie; B. Gao, K. Xu. The

Mechanism of Capacity Decay in $LiFePO_4$/Graphite Batteries at Different State of Health. *Renewables* **2025**, *3*, 346-356.

[24] Xue, L.; Q. Zhang; Y. Huang; H. Zhu; L. Xu; S. Guo; X. Zhu; H. Liu; Y. Huang; J. Huang; L. Lu; S. Zhang; L. Gu; Q. Liu; J. Zhu, H. Xia. Stabilizing Layered Structure in Aqueous Electrolyte via Dynamic Water Intercalation/Deintercalation. *Adv. Mater.* **2022**, *34*, 2108541.

[25] Adebanjo, I.T.; J. Eko; A.G. Agbeyegbe; S.F. Yuk; S.V. Cowart; E.A. Nagelli; F.J. Burpo; J.L. Allen; D.T. Tran; N. Bhattarai; K. Shah; J.-Y. Hwang, H.H. Sun. A comprehensive review of lithium-ion battery components degradation and operational considerations: a safety perspective. *Energy Adv.* **2025**, *4*, 820-877.

[26] Zhao, Q.; S. Zhang; T. Li; C. Xu; J. Yang; B. Qu; H. Zhou; T. Feng, M. Wu. Enhanced Electrochemical Delithiation of $LiFePO_4$ in a Composite Aqueous Electrolyte for High-Performance Olivine $FePO_4$. *J. Electrochem. Soc.* **2023**, *170*, 040521.

[27] Gopinadh, S.V.; P.V.R.L. Phanendra; B. John, T.D. Mercy. Aqueous rechargeable lithium ion batteries – Yesterday, today and tomorrow. *J. Energy Storage* **2025**, *132*, 117829.

[28] Lüchtefeld, J.; M.-Y. Lee; H. Hemmelmann; S. Wachs; C. Behling; K.J.J. Mayrhofer; M.T. Elm, B.B. Berkes. Contribution of Electrolyte Decomposition Products and the Effect of Temperature on the Dissolution of Transition Metals from Cathode Materials. *ACS Omega* **2023**, *8*, 32606-32614.

[29] Rikka, V.R.; S.R. Sahu; M. Gurumurthy; A. Chatterjee; S. Chandran; G. Sundararajan; R. Gopalan, R. Prakash. Temperature-Derived Fe Dissolution of a $LiFePO_4$/Graphite Cell at Fast Charging and High State-of-Charge Condition. *Energy Technol.* **2023**, *11*, 2201388.

[30] Quan, Y.; S. Li; N. Zhang; X. Cui; D. Zhao; Y. Zhang; M. Wang, X. Li. Improving performances of cathode-electrolyte interphase via the potentiostatic reduction of lithium bis(fluorosulfonyl)imide additive. *Electrochim. Acta* **2023**, *460*, 142617.

[31] Kaur, A.; H. Wang; U. Gulzar; C. O'Dwyer, A.P. O'Mullane. Using Recovered Lithium Iron Phosphate Battery Materials as Efficient Electrocatalysts for the Oxygen Evolution Reaction. *CleanMat* **2025**, *2*, 155-167.

[32] Fu, J.; K. Wang; D. Liu; Z. Zhang; M. Sui, P. Yan. b-Axis Phase Boundary Movement Induced (020) Plane Cracking in $LiFePO_4$. *ACS Appl. Mater. Interfaces* **2020**, *12*, 39245-39251.

[33] Huang, M.; M. Wang; L. Yang; Z. Wang; H. Yu; K. Chen; F. Han; L. Chen; C. Xu; L. Wang; P. Shao, X. Luo. Direct Regeneration of Spent Lithium-Ion Battery Cathodes: From Theoretical Study to Production Practice. *Nano-Micro Lett.* **2024**, *16*, 207.

[34] Zhao, X.; H. Chen; H. Wu; Y. Zhao, J. Luo. Nondisassembly Repair of Degraded $LiFePO_4$ Cells via Lithium Restoration from the Solid Electrolyte Interphase. *ACS Nano* **2024**, *18*, 21125-21134.

[35] Kumar, S.; P. Chand; A. Kumar, H. Anand. Effect of different aqueous electrolytes on electrochemical behavior of $LiFePO_4$ as a cathode material: Lithium ion battery and renewable energy nexus. *Energy Nexus* **2021**, *1*, 100005.

[36] Zhang, X.; P. Xing; T.L. Madanu; J. Li; J. Shu, B.L. Su. Aqueous batteries: from laboratory to market. *Natl. Sci. Rev.* **2023**, *10*, nwad235.

[37] Zheng, J.; G. Tan; P. Shan; T. Liu; J. Hu; Y. Feng; L. Yang; M. Zhang; Z. Chen; Y. Lin; J. Lu; J.C. Neuefeind; Y. Ren; K. Amine; L.-W. Wang; K. Xu, F. Pan. Understanding Thermodynamic and Kinetic Contributions in Expanding the Stability Window of Aqueous Electrolytes. *Chem* **2018**, *4*, 2872-2882.

[38] Jiang, L.; Y. Lu; C. Zhao; L. Liu; J. Zhang; Q. Zhang; X. Shen; J. Zhao; X. Yu; H. Li; X. Huang; L. Chen, Y.-S. Hu. Building aqueous K-ion batteries for energy storage. *Nat. Energy* **2019**, *4*, 495-503.

[39] Zhang, H.; X. Liu; H. Li; I. Hasa, S. Passerini. Challenges and Strategies for High-Energy Aqueous Electrolyte Rechargeable Batteries. *Angew. Chem., Int. Ed.* **2021**, *60*, 598-616.

[40] Wu, J.; W. Cai, G. Shang. In situ Electrochemical-AFM Study of $LiFePO_4$ Thin Film in Aqueous Electrolyte. *Nanoscale Res. Lett.* **2016**, *11*, 223.

[41] Liang, Y., Y. Yao. Designing modern aqueous batteries. *Nat. Rev. Mater.* **2023**, *8*, 109-122.

[42] Wang, Y.; Z. Feng; D. Laul; W. Zhu; M. Provencher; M.L. Trudeau; A. Guerfi, K. Zaghib. Ultra-low cost and highly stable hydrated $FePO_4$ anodes for aqueous sodium-ion battery. *J. Power Sources* **2018**, *374*, 211-216.

[43] Zhang, Y.; P. Xin, Q. Yao. Electrochemical performance of $LiFePO_4$/C synthesized by sol-gel method as cathode for aqueous lithium ion batteries. *J. Alloys Compd.* **2018**, *741*, 404-408.

[44] Li, C.-C.; S.-J. Chang, C.-A. Chen. Effects of sp^2- and sp^3-carbon coatings on dissolution and electrochemistry of water-based $LiFePO_4$ cathodes. *J. Appl. Electrochem.* **2017**, *47*,

1065-1072.

[45] Sahivirta, H.; A. Santasalo-Aarnio, R. Serna-Guerrero. A corrosion study of lithium-ion batteries during NaCl electrochemical discharge: mechanistic origins and Zn-based mitigation strategies. *Sustainable Energy Fuels* **2026**, *10*, 2110-2125.

[46] Li, C.-C.; X.-W. Peng; J.-T. Lee, F.-M. Wang. Using Poly(4-Styrene Sulfonic Acid) to Improve the Dispersion Homogeneity of Aqueous-Processed $LiFePO_4$ Cathodes. *J. Electrochem. Soc.* **2010**, *157*, A517.

[47] Lee, J.-H.; H.-H. Kim; G.-S. Kim; D.-S. Zang; Y.-M. Choi; H. Kim; D.K. Yi; W.M. Sigmund, U. Paik. Evaluation of Surface Acid and Base Properties of $LiFePO_4$ in Aqueous Medium with pH and Its Electrochemical Properties. *J. Phys. Chem. C* **2010**, *114*, 4466-4472.

[48] Noerochim, L.; A.O. Yurwendra, D. Susanti. Effect of carbon coating on the electrochemical performance of $LiFePO_4$/C as cathode materials for aqueous electrolyte lithium-ion battery. *Ionics* **2016**, *22*, 341-346.

[49] Yan, J.; J. Qian; Y. Li; L. Li; F. Wu, R. Chen. Toward Sustainable Lithium Iron Phosphate in Lithium-Ion Batteries: Regeneration Strategies and Their Challenges. *Adv. Funct. Mater.* **2024**, *34*, 2405055.

[50] Lai, Y.; Z. Cao; H. Song; Z. Zhang; X. Chen; H. Lu; M. Jia, J. Li. Influence of Fe (II) Species in Electrolyte on Performance of Graphite Anode for Lithium-Ion Batteries. *J. Electrochem. Soc.* **2012**, *159*, A1961.

[51] Joshi, T.; K. Eom; G. Yushin, T.F. Fuller. Effects of Dissolved Transition Metals on the Electrochemical Performance and SEI Growth in Lithium-Ion Batteries. *J. Electrochem. Soc.* **2014**, *161*, A1915.

[52] Li, D.; D. L. Danilov; L. Gao; Y. Yang, P.H.L. Notten. Degradation Mechanisms of C_6/$LiFePO_4$ Batteries: Experimental Analyses of Cycling-induced Aging. *Electrochim. Acta* **2016**, *210*, 445-455.

[53] Zhu, W.; W. Xu; D. Liu; L. He, Z. Zhao. Extending $LiFePO_4$ electrode lifespan for electrochemical lithium extraction from brines: A deep (de)intercalation-driven regeneration strategy targeting impurity cations co-insertion. *Desalination* **2025**, *614*, 119166.

[54] Kim, N.; X. Su, C. Kim. Electrochemical lithium recovery system through the simultaneous lithium enrichment via sustainable redox reaction. *Chem. Eng. J.* **2021**, *420*, 127715.

[55] Gilbert, J.A.; I.A. Shkrob, D.P. Abraham. Transition Metal Dissolution, Ion Migration, Electrocatalytic Reduction and Capacity Loss in Lithium-Ion Full Cells. *J. Electrochem. Soc.* **2017**, *164*, A389.

[56] Dreyer, W.; J. Jamnik; C. Guhlke; R. Huth; J. Moškon, M. Gaberšček. The thermodynamic origin of hysteresis in insertion batteries. *Nat. Mater.* **2010**, *9*, 448-453.

[57] Owen, J., A. Hector. Phase-transforming electrodes. *Science* **2014**, *344*, 1451-1452.

[58] Cogswell, D.A., M.Z. Bazant. Coherency Strain and the Kinetics of Phase Separation in $LiFePO_4$ Nanoparticles. *ACS Nano* **2012**, *6*, 2215-2225.

[59] Burch, D.; G. Singh; G. Ceder, M.Z. Bazant. Phase-Transformation Wave Dynamics in $LiFePO_4$. *Solid State Phenom.* **2008**, *139*, 95-100.

[60] Chen, G.; X. Song, T.J. Richardson. Electron Microscopy Study of the $LiFePO_4$ to $FePO_4$ Phase Transition. *Electrochem. Solid-State Lett.* **2006**, *9*, A295.

[61] Zhang, B.; S. Wang; Y. Li; P. Sun; C. Yang; D. Wang, L. Liu. Review: Phase transition mechanism and supercritical hydrothermal synthesis of nano lithium iron phosphate. *Ceram. Int.* **2020**, *46*, 27922-27939.

[62] Yan, G.; J. Wei; E. Apodaca; S. Choi; P.J. Eng; J.E. Stubbs; Y. Han; S. Zou; M.K. Bera; R. Wu; E. Karapetrova; H. Zhou; W. Chen, C. Liu. Identifying critical features of iron phosphate particle for lithium preference. *Nat. Commun.* **2024**, *15*, 4859.

[63] Hou, X.; X. Ju; W. Zhao; J. Wang; X. He; L. Du; B. Yan; J. Li; E. Paillard; J. Sun; H. Lin; M. Winter, J. Li. TiO_2@$LiTi_2(PO_4)_3$ enabling fast and stable lithium storage for high voltage aqueous lithium-ion batteries. *J. Power Sources* **2021**, *484*, 229255.

[64] Oh, H.; S.-J. Shin; E. Choi; H. Yamagishi; T. Ohta; N. Yabuuchi; H.-G. Jung; H. Kim, H.R. Byon. Anion-Induced Interfacial Liquid Layers on $LiCoO_2$ in Salt-in-Water Lithium-Ion Batteries. *JACS Au* **2023**, *3*, 1392-1402.

[65] Tron, A.; Y.N. Jo; S.H. Oh; Y.D. Park, J. Mun. Surface Modification of the $LiFePO_4$ Cathode for the Aqueous Rechargeable Lithium Ion Battery. *ACS Appl. Mater. Interfaces* **2017**, *9*, 12391-12399.

[66] Yang, Y.; J. Wang; H. Luo; X.-w. Yu; Y. Lin; Y. Ru; Z. Liu; P. Wang; Y. Gong; J. Li; H. Wang; Y. Zou; Y. Qiao; H. Zhou, S.J.J.o.t.A.C.S. Sun. From Interphase to Interface: Revealing the Dynamic Evolution of Interfacial Electrolyte Configuration and Solid Electrolyte Interphase on Lithium Metal Anode at Elevated Temperature. *J. Am. Chem. Soc.*

2026, *148*, 12073-12087.

[67] Huang, L.; D. Bao; Y. Jiang; K. Regenauer-Lieb; Y. Zheng, S.-Z. Qiao. The utilization of ions in seawater for electrocatalysis. *Natl. Sci. Rev.* **2025**, *12*, nwaf461.

[68] Cao, Y.; S. Ju; Q. Zhang; K. Gao; A. Marcelli, Z. Zhang. Recent progress in aqueous zinc-ion batteries based on conversion-type cathodes. *Adv. Powder Mater.* **2025**, *4*, 100278.

[69] Li, X.; H. Yu; D.A. Alshammari; S. Tian; G. Chen; K. Xi; H.K. Thabet; B. Lu; Z.M. El-Bahy; Y. Liu; Y. Chen, J. Zhou. Regulation of Proton Vehicle Migration for Synergetic Interfacial Stability Enables Long-Lasting Ah-Level Zinc-Ion Batteries. *Adv. Mater.* **2026**, *38*, e16427.

[70] Pérez-Rodríguez, S.; S.D.S. Fitch; P.N. Bartlett, N. Garcia-Araez. $LiFePO_4$ Battery Material for the Production of Lithium from Brines: Effect of Brine Composition and Benefits of Dilution. *ChemSusChem* **2022**, *15*, e202102182.

[71] Yang, Z.; Y. Dai; S. Wang, J. Yu. How to make lithium iron phosphate better: a review exploring classical modification approaches in-depth and proposing future optimization methods. *J. Mater. Chem. A* **2016**, *4*, 18210-18222.

[72] Xie, L.; J. Zhou; D. Wang; Y. Li; X. He; Y. Wu, Y. Deng. Stabilizing Electrode/Electrolyte interphases for Lithium-Ion batteries at High-Temperature through integrated electrolyte engineering and surface modification. *Mater. Today* **2026**, *96*, 103303.

[73] Yamamoto, C.; A. Ikezawa; T. Okajima, H. Arai. Phase Transition Kinetics of $LiFePO_4$ Biphasic Systems in Aqueous and Non-aqueous Electrolytes. *Electrochemistry* **2024**, *92*, 027001.

[74] Chung, S.-Y.; J.T. Bloking, Y.-M. Chiang. Electronically conductive phospho-olivines as lithium storage electrodes. *Nat. Mater.* **2002**, *1*, 123-128.

[75] Xiao, Y.; Z. Zhao; Q. Zhang, R. Qiao. Doping $LiFePO_4$ with Al^{3+}: Suppression of Anti-Site Defects and Implications for Battery Recycling. *ACS Omega* **2025**, *10*, 1293-1302.

[76] Koltypin, M.; D. Aurbach; L. Nazar, B. Ellis. On the Stability of $LiFePO_4$ Olivine Cathodes under Various Conditions (Electrolyte Solutions, Temperatures). *Electrochem. Solid-State Lett.* **2007**, *10*, A40.

[77] Jiang, K.; F. Wang; M. Liu; Y. Fan; Z. Chen; G. Li; P. Li; X. Shi, W. Hong. First principles study of the electronic structure and Li-ion diffusion properties of co-doped $LIFe_{x-1}M_xP_yN_{y-1}O_4$ (M=Co/Mn, NS/Si) Li-ion battery cathode materials. *Micro Nanostruct.* **2024**, *196*, 207988.

[78] Zhang, B.; Y. He; H. Gao; X. Wang; J. Liu; H. Xu; L. Wang, X. He. Unraveling the doping mechanisms in lithium iron phosphate. *Energy Mater.* **2022**, *2*, 200013.

[79] Islam, M.S.; D.J. Driscoll; C.A.J. Fisher, P.R. Slater. Atomic-Scale Investigation of Defects, Dopants, and Lithium Transport in the $LiFePO_4$ Olivine-Type Battery Material. *Chem. Mater.* **2005**, *17*, 5085-5092.

[80] Liu, Y.; W. Qin; D. Zhang; L. Feng, L. Wu. Effect of Na^+ in situ doping on $LiFePO_4$/C cathode material for lithium-ion batteries. *Prog. Nat. Sci.: Mater. Int.* **2021**, *31*, 14-18.

[81] Johnson, I.D.; E. Blagovidova; P.A. Dingwall; D.J.L. Brett; P.R. Shearing, J.A. Darr. High power Nb-doped $LiFePO_4$ Li-ion battery cathodes; pilot-scale synthesis and electrochemical properties. *J. Power Sources* **2016**, *326*, 476-481.

[82] Kulka, A.; A. Braun; T.-W. Huang; A. Wolska; M.T. Klepka; A. Szewczyk; D. Baster; W. Zając; K. Świerczek, J. Molenda. Evidence for Al doping in lithium sublattice of $LiFePO_4$. *Solid State Ionics* **2015**, *270*, 33-38.

[83] Zaghib, K.; M. Dontigny; A. Guerfi; P. Charest; I. Rodrigues; A. Mauger, C.M. Julien. Safe and fast-charging Li-ion battery with long shelf life for power applications. *J. Power Sources* **2011**, *196*, 3949-3954.

[84] Yamada, A.; S.C. Chung, K. Hinokuma. Optimized $LiFePO_4$ for Lithium Battery Cathodes. *J. Electrochem. Soc.* **2001**, *148*, A224.

[85] Zhang, H.; Y. Tang; J. Shen; X. Xin; L. Cui; L. Chen; C. Ouyang; S. Shi, L. Chen. Antisite defects and Mg doping in $LiFePO_4$: a first-principles investigation. *Appl. Phys. A* **2011**, *104*, 529-537.

[86] Naik, A., S.C. P. Microwave synthesis of molybdenum doped $LiFePO_4$/C and its electrochemical studies. *Dalton Trans.* **2016**, *45*, 8021-8027.

[87] Ma, G.; X. Luo; M. Cheng, D. Ju. Effect of impurities in $FePO_4$ raw materials on the performance of $LiFePO_4$ cathode materials. *Sci. Rep.* **2025**, *15*, 15122.

[88] Shen, C.; W. Lin; H. Hu; P. Yang, L. Wang. The electronic and geometric structure modifications of $LiFePO_4$ with vanadium doping to achieve ultrafast discharging capability: The experimental and theoretical investigations. *J. Alloys Compd.* **2023**, *936*, 168035.

[89] Zeng, Z.; H. Lei; X. Lu; C. Zhu; Y. Wen; J. Zhu; X. Ji; W. Sun; Y. Yang, P. Ge. Li-Fe anti-sites defects in $LiFePO_4$: Mechanism, characterization and cathode-regeneration

applications. *Energy Stor. Mater.* **2025**, *74*, 103947.

[90] Goonetilleke, D.; T. Faulkner; V.K. Peterson, N. Sharma. Structural evidence for Mg-doped $LiFePO_4$ electrode polarisation in commercial Li-ion batteries. *J. Power Sources* **2018**, *394*, 1-8.

[91] Zhang, Y.; Z. Shao, Y. Zhang. Preparation of Mo-doping $LiFePO_4$/C by carbon reduction method. *Mater. Manuf. Processes* **2021**, *36*, 419-425.

[92] Johnson, I.D.; M. Lübke; O.Y. Wu; N.M. Makwana; G.J. Smales; H.U. Islam; R.Y. Dedigama; R.I. Gruar; C.J. Tighe; D.O. Scanlon; F. Corà; D.J.L. Brett; P.R. Shearing, J.A. Darr. Pilot-scale continuous synthesis of a vanadium-doped $LiFePO_4$/C nanocomposite high-rate cathodes for lithium-ion batteries. *J. Power Sources* **2016**, *302*, 410-418.

[93] Lee, H.; S. Kim; N.S. Parmar; J.-H. Song; K.-y. Chung; K.-B. Kim, J.-W. Choi. Carbon-free Mn-doped $LiFePO_4$ cathode for highly transparent thin-film batteries. *J. Power Sources* **2019**, *434*, 226713.

[94] Kim, S.; V. Mathew; J. Kang; J. Gim; J. Song; J. Jo, J. Kim. High rate capability of $LiFePO_4$ cathodes doped with a high amount of Ti. *Ceram. Int.* **2016**, *42*, 7230-7236.

[95] Guo, X.; M. Wang; X. Huang; P. Zhao; X. Liu, R. Che. Direct evidence of antisite defects in $LiFe_{0.5}Mn_{0.5}PO_4$ via atomic-level HAADF-EELS. *J. Mater. Chem. A* **2013**, *1*, 8775-8781.

[96] Xue, J.; Y. Wang; J. Lin; X. Ke, G. Liang. The influence of iron site doping lithium iron phosphate on the low temperature properties and the diffusion mechanism of lithium ion. *Ionics* **2024**, *30*, 7939-7951.

[97] Jugović, D.; M. Mitrić; M. Milović; N. Cvjetićanin; B. Jokić; A. Umićević, D. Uskoković. The influence of fluorine doping on the structural and electrical properties of the $LiFePO_4$ powder. *Ceram. Int.* **2017**, *43*, 3224-3230.

[98] Zaki, N.H.M.; S.I. Ahmad; F.N. Sazman; F.W. Badrudin; A.L.A. Abdullah; M.F.M. Taib; O.H. Hassan, M.Z.A. Yahya. The influence of Cl doping on the structural, electronic properties and Li-ion migration of $LiFePO_4$: A DFT study. *Comput. Theor. Chem.* **2023**, *1221*, 114029.

[99] Liao, X.-Z.; Y.-S. He; Z.-F. Ma; X.-M. Zhang, L. Wang. Effects of fluorine-substitution on the electrochemical behavior of $LiFePO_4$/C cathode materials. *J. Power Sources* **2007**, *174*, 720-725.

[100] Li, X.; Z. Shao; K. Liu; Q. Zhao; G. Liu, B. Xu. Effect of F-doping on the properties of $LiFePO_{4-x}/3F_x$/C cathode materials via wet mechanical agitation-assisted high-temperature ball milling method. *J. Solid State Electrochem.* **2018**, *22*, 2837-2843.

[101] Gao, C.; J. Zhou; G. Liu, L. Wang. Synthesis of F-doped $LiFePO_4$/C cathode materials for high performance lithium-ion batteries using co-precipitation method with hydrofluoric acid source. *J. Alloys Compd.* **2017**, *727*, 501-513.

[102] Sun, C.S.; Y. Zhang; X.J. Zhang, Z. Zhou. Structural and electrochemical properties of Cl-doped $LiFePO_4$/C. *J. Power Sources* **2010**, *195*, 3680-3683.

[103] Wang, Z.; X. Kong; Z. Fan; S. Ding; Q. Rong, Y. Su. A First-Principles Study of Anion Doping in $LiFePO_4$ Cathode Materials for Li-Ion Batteries. *ChemPhysChem* **2024**, *25*, e202300756.

[104] Xu, G.; K. Zhong; J.-M. Zhang, Z. Huang. First-principles study of structural, electronic and Li-ion diffusion properties of N-doped $LiFePO_4$ (010) surface. *Solid State Ionics* **2015**, *281*, 1-5.

[105] Trócoli, R.; S. Franger; M. Cruz; J. Morales, J. Santos-Peña. Improving the electrochemical properties of nanosized $LiFePO_4$-based electrode by boron doping. *Electrochim. Acta* **2014**, *135*, 558-567.

[106] Li, Y.; L. Wang; F. Liang; Y. Yao, K. Zhang. Enhancing high rate performance and cyclability of $LiFePO_4$ cathode materials for lithium ion batteries by boron doping. *J. Alloys Compd.* **2021**, *880*, 160560.

[107] Okada, K.; I. Kimura, K. Machida. High rate capability by sulfur-doping into $LiFePO_4$ matrix. *RSC Adv.* **2018**, *8*, 5848-5853.

[108] Liu, H.; S.-h. Luo; S.-x. Yan; Y.-f. Wang; Q. Wang; M.-q. Li, Y.-h. Zhang. A novel and low-cost iron source for synthesizing Cl-doped $LiFePO_4$/C cathode materials for lithium-ion batteries. *J. Electroanal. Chem.* **2019**, *850*, 113434.

[109] Aguiló-Aguayo, N.; D. Hubmann; F.U. Khan; S. Arzbacher, T. Bechtold. Water-based slurries for high-energy $LiFePO_4$ batteries using embroidered current collectors. *Sci. Rep.* **2020**, *10*, 5565.

[110] Song, J.; B. Sun; H. Liu; Z. Ma; Z. Chen; G. Shao, G. Wang. Enhancement of the Rate Capability of $LiFePO_4$ by a New Highly Graphitic Carbon-Coating Method. *ACS Appl. Mater. Interfaces* **2016**, *8*, 15225-15231.

[111] Liu, Y.; J. Wang; J. Liu; M.N. Banis; B. Xiao; A. Lushington; W. Xiao; R. Li; T.-K. Sham; G. Liang, X. Sun. Origin of phase inhomogeneity in lithium iron phosphate during carbon coating. *Nano Energy* **2018**, *45*, 52-60.

[112] Park, S.; J. Oh; J.M. Kim; V. Guccini; T. Hwang; Y. Jeon; G. Salazar-Alvarez, Y. Piao. Facile preparation of cellulose nanofiber derived carbon and reduced graphene oxide co-supported LiFePO4 nanocomposite as enhanced cathode material for lithium-ion battery. *Electrochim. Acta* **2020**, *354*, 136707.

[113] Yan, X.; Y. Yang; C. Li; J. Liu; J. Wang; F. Xi; T. Wang, W. He. The synthesis of $LiFePO_4$/C with polyaniline as coated carbon source and sucrose as reducing carbon source. *Ionics* **2022**, *28*, 1559-1571.

[114] Huang, Y.-G.; F.-H. Zheng; X.-H. Zhang; Q.-Y. Li, H.-Q. Wang. Effect of carbon coating on cycle performance of $LiFePO_4$/C composite cathodes using Tween80 as carbon source. *Electrochim. Acta* **2014**, *130*, 740-747.

[115] Choi, J.; O. Zabihi; M. Ahmadi, M. Naebe. Advancing structural batteries: cost-efficient high-performance carbon fiber-coated $LiFePO_4$ cathodes. *RSC Adv.* **2023**, *13*, 30633-30642.

[116] Liu, Y.; J. Liu; J. Wang; M.N. Banis; B. Xiao; A. Lushington; W. Xiao; R. Li; T.-K. Sham; G. Liang, X. Sun. Formation of size-dependent and conductive phase on lithium iron phosphate during carbon coating. *Nat. Commun.* **2018**, *9*, 929.

[117] Wang, P.; G. Zhang; Z. Li; W. Sheng; Y. Zhang; J. Gu; X. Zheng, F. Cao. Improved Electrochemical Performance of $LiFePO_4$@N-Doped Carbon Nanocomposites Using Polybenzoxazine as Nitrogen and Carbon Sources. *ACS Appl. Mater. Interfaces* **2016**, *8*, 26908-26915.

[118] Wang, X.; Z. Feng; X. Hou; L. Liu; M. He; X. He; J. Huang, Z. Wen. Fluorine doped carbon coating of $LiFePO_4$ as a cathode material for lithium-ion batteries. *Chem. Eng. J.* **2020**, *379*, 122371.

[119] Li, F.; R. Tao; X. Tan; J. Xu; D. Kong; L. Shen; R. Mo; J. Li, Y. Lu. Graphite-Embedded Lithium Iron Phosphate for High-Power–Energy Cathodes. *Nano Lett.* **2021**, *21*, 2572-2579.

[120] Wang, B.; W. Al Abdulla; D. Wang, X.S. Zhao. A three-dimensional porous $LiFePO_4$ cathode material modified with a nitrogen-doped graphene aerogel for high-power lithium ion batteries. *Energy Environ. Sci.* **2015**, *8*, 869-875.

[121] Ventrapragada, L.K.; J. Zhu; S.E. Creager; A.M. Rao, R. Podila. A Versatile Carbon Nanotube-Based Scalable Approach for Improving Interfaces in Li-Ion Battery Electrodes. *ACS Omega* **2018**, *3*, 4502-4508.

[122] Wu, X.-L.; Y.-G. Guo; J. Su; J.-W. Xiong; Y.-L. Zhang, L.-J. Wan. Carbon-Nanotube-Decorated Nano-$LiFePO_4$ @C Cathode Material with Superior High-Rate and Low-Temperature Performances for Lithium-Ion Batteries. *Adv. Energy Mater.* **2013**, *3*, 1155-1160.

[123] Fan, J.; J. Chen; Y. Chen; H. Huang; Z. Wei; M.-s. Zheng, Q. Dong. Hierarchical structure $LiFePO_4$@C synthesized by oleylamine-mediated method for low temperature applications. *J. Mater. Chem. A* **2014**, *2*, 4870-4873.

[124] Zhou, X.; F. Wang; Y. Zhu, Z. Liu. Graphene modified $LiFePO_4$ cathode materials for high power lithium ion batteries. *J. Mater. Chem.* **2011**, *21*, 3353-3358.

[125] Wang, H.; S. Liu, Y. Huang. Preparation and characterization of SnO_2 and Carbon Co-coated $LiFePO_4$ cathode materials. *J. Nanosci. Nanotechnol.* **2014**, *14*, 3281-3283.

[126] Liu, S.; H. Yin; H. Wang; J. He, H. Wang. Synthesis, characterization and electrochemical performances of MoO_2 and carbon co-coated $LiFePO_4$ cathode materials. *Ceram. Int.* **2014**, *40*, 3325-3331.

[127] Liu, S., H. Wang. WO_2 modified $LiFePO_4$/C cathode materials with improved electrochemical performance synthesized by in-situ synthesis method. *Mater. Lett.* **2014**, *122*, 151-154.

[128] Zhang, M.; N. Garcia-Araez; A.L. Hector, J.R. Owen. A sol-gel route to titanium nitride conductive coatings on battery materials and performance of TiN-coated $LiFePO_4$. *J. Mater. Chem. A* **2017**, *5*, 2251-2260.

[129] Zhong, S.; L. Wu, J. Liu. Sol-gel synthesis and electrochemical properties of $9LiFePO_4 \cdot Li_3V_2(PO_4)_3$/C composite cathode material for lithium ion batteries. *Electrochim. Acta* **2012**, *74*, 8-15.

[130] Liang, S.; X. Cao; Y. Wang; Y. Hu; A. Pan, G. Cao. Uniform $8LiFePO_4 \cdot Li_3V_2(PO_4)_3$/C nanoflakes for high-performance Li-ion batteries. *Nano Energy* **2016**, *22*, 48-58.

[131] Zhao, S.-X.; H. Ding; Y.-C. Wang; B.-H. Li, C.-W. Nan. Improving rate performance of $LiFePO_4$ cathode materials by hybrid coating of nano-Li_3PO_4 and carbon. *J. Alloys Compd.* **2013**, *566*, 206-211.

[132] Shu, H.; M. Chen; Y. Fu; X. Yang; X. Yi; Y. Bai; Q. Liang; Q. Wei; B. Hu; J. Tan; C. Wu; M. Zhou, X. Wang. Improvement of electrochemical performance for spherical $LiFePO_4$ via hybrid coated with electron conductive carbon and fast Li ion conductive $La_{0.56}Li_{0.33}TiO_3$. *J. Power Sources* **2014**, *252*, 73-78.

[133] Luo, L.; F. Zheng; H. Gao; C. Lan; Z. Sun; W. Huang; X. Han; Z. Zhang; P. Su; P. Wang; S. Guo; G. Lin; J. Xu; J. Wang; J. Li; C. Li; Q. Zhang; S. Wu; M.-S. Wang, S. Chen. Tuning the

electron transport behavior at Li/LATP interface for enhanced cyclability of solid-state Li batteries. *Nano Res.* **2023**, *16*, 1634-1641.

[134] Shu, H.; M. Chen; F. Wen; Y. Fu; Q. Liang; X. Yang; Y. Shen; L. Liu, X. Wang. Li fast ion conductive $La_{0.56}Li_{0.33}TiO_3$ inlaid $LiFePO_4$/C microspheres with enhanced high-rate performance as cathode materials. *Electrochim. Acta* **2015**, *152*, 368-377.

[135] Malik, R.; D. Burch; M. Bazant, G. Ceder. Particle Size Dependence of the Ionic Diffusivity. *Nano Lett.* **2010**, *10*, 4123-4127.

[136] Delacourt, C.; P. Poizot; S. Levasseur, C. Masquelier. Size Effects on Carbon-Free $LiFePO_4$ Powders: The Key to Superior Energy Density. *Electrochem. Solid-State Lett.* **2006**, *9*, A352.

[137] Lee, M.-H.; T.-H. Kim; Y.S. Kim; J.-S. Park, H.-K. Song. Optimized evolution of a secondary structure of $LiFePO_4$: balancing between shape and impurities. *J. Mater. Chem.* **2012**, *22*, 8228-8234.

[138] Wang, L.; F. Zhou, G. Ceder. Ab Initio Study of the Surface Properties and Nanoscale Effects of $LiMnPO_4$. *Electrochem. Solid-State Lett.* **2008**, *11*, A94.

[139] Yang, S.; M. Hu; L. Xi; R. Ma; Y. Dong, C.Y. Chung. Solvothermal Synthesis of Monodisperse $LiFePO_4$ Micro Hollow Spheres as High Performance Cathode Material for Lithium Ion Batteries. *ACS Appl. Mater. Interfaces* **2013**, *5*, 8961-8967.

[140] Sarmadi, A.; S.M. Masoudpanah, S. Alamolhoda. L-Lysine-assisted solvothermal synthesis of hollow-like structure $LiFePO_4$/C powders as cathode materials for Li-ion batteries. *J. Mater. Res. Technol.* **2021**, *15*, 5405-5413.

[141] Zheng, Z.; W.K. Pang; X. Tang; D. Jia; Y. Huang, Z. Guo. Solvothermal synthesis and electrochemical performance of hollow $LiFePO_4$ nanoparticles. *J. Alloys Compd.* **2015**, *640*, 95-100.

[142] Du, G.; Y. Zhou; X. Tian; G. Wu; Y. Xi, S. Zhao. High-performance 3D directional porous $LiFePO_4$/C materials synthesized by freeze casting. *Appl. Surf. Sci.* **2018**, *453*, 493-501.

[143] Du, J.; L.-B. Kong; H. Liu; J.-B. Liu; M.-C. Liu; P. Zhang; Y.-C. Luo, L. Kang. Template-free synthesis of porous–$LiFePO_4$/C nanocomposite for high power lithium-ion batteries. *Electrochim. Acta* **2014**, *123*, 1-6.

[144] Guo, B.; H. Ruan; C. Zheng; H. Fei, M. Wei. Hierarchical $LiFePO_4$ with a controllable growth of the (010) facet for lithium-ion batteries. *Sci. Rep.* **2013**, *3*, 2788.

[145] Jiang, N.; Y. Zeng; Q. Yang; P. Lu; K. Qu; L. Ye; X. Lu; Z. Liu; X. Li; Y. Tang; J. Cao; S. Chen; C. Zhi, J. Qiu. Deep ion mass transfer addressing the capacity shrink challenge of aqueous Zn|MnO2 batteries during the cathode scaleup. *Energy Environ. Sci.* **2024**, *17*, 8904-8914.

[146] Diaz-Lopez, M.; P.A. Chater; P. Bordet; M. Freire; C. Jordy; O.I. Lebedev, V. Pralong. Li_2O:Li-Mn-O Disordered Rock-Salt Nanocomposites as Cathode Prelithiation Additives for High-Energy Density Li-Ion Batteries. *Adv. Energy Mater.* **2020**, *10*, 1902788.

[147] Sun, Y.; H.-W. Lee; Z.W. Seh; N. Liu; J. Sun; Y. Li, Y. Cui. High-capacity battery cathode prelithiation to offset initial lithium loss. *Nat. Energy* **2016**, *1*, 15008.

[148] Sun, Y.; H.-W. Lee; G. Zheng; Z.W. Seh; J. Sun; Y. Li, Y. Cui. In Situ Chemical Synthesis of Lithium Fluoride/Metal Nanocomposite for High Capacity Prelithiation of Cathodes. *Nano Lett.* **2016**, *16*, 1497-1501.

[149] Ren, Z.; X. Shi, Z.-S. Wu. Recent advancements and next of aqueous rechargeable lithium-ion batteries. *Next Energy* **2023**, *1*, 100068.

[150] Sun, D.; Y. Jiang; H. Wang; Y. Yao; G. Xu; K. He; S. Liu; Y. Tang; Y. Liu, X. Huang. Advanced aqueous rechargeable lithium battery using nanoparticulate $LiTi_2(PO_4)_3$/C as a superior anode. *Sci. Rep.* **2015**, *5*, 10733.

[151] Dong, X.; L. Chen; X. Su; Y. Wang, Y. Xia. Flexible Aqueous Lithium-Ion Battery with High Safety and Large Volumetric Energy Density. *Angew. Chem., Int. Ed.* **2016**, *55*, 7474-7477.

[152] Droguet, L.; A. Grimaud; O. Fontaine, J.-M. Tarascon. Water-in-Salt Electrolyte (WiSE) for Aqueous Batteries: A Long Way to Practicality. *Adv. Energy Mater.* **2020**, *10*, 2002440.

[153] Chen, L.; J. Zhang; Q. Li; J. Vatamanu; X. Ji; T.P. Pollard; C. Cui; S. Hou; J. Chen; C. Yang; L. Ma; M.S. Ding; M. Garaga; S. Greenbaum; H.-S. Lee; O. Borodin; K. Xu, C. Wang. A 63 m Superconcentrated Aqueous Electrolyte for High-Energy Li-Ion Batteries. *ACS Energy Lett.* **2020**, *5*, 968-974.

[154] Nian, Q.; X. Zhang; Y. Feng; S. Liu; T. Sun; S. Zheng; X. Ren; Z. Tao; D. Zhang, J. Chen. Designing Electrolyte Structure to Suppress Hydrogen Evolution Reaction in Aqueous Batteries. *ACS Energy Lett.* **2021**, *6*, 2174-2180.

[155] Tron, A.; S. Jeong; Y.D. Park, J. Mun. Aqueous Lithium-Ion Battery of Nano-$LiFePO_4$ with Antifreezing Agent of Ethyleneglycol for Low-Temperature Operation. *ACS*

Sustainable Chem. Eng. **2019**, *7*, 14531-14538.

Meng Yao received his B.S. degree in Chemical Engineering from Tsinghua University in 2017 and his Ph.D. degree from the Institute of Process Engineering, Chinese Academy of Sciences in 2022 He is currently a Distinguished Associate Researcher and Master's Supervisor at Sichuan University. He has published 35 SCI papers as first/corresponding author in prestigious journals including Advanced Materials, Angewandte Chemie International Edition, Energy & Environmental Science, Advanced Energy Materials, with an H-index of 24 and over 2000 total citations. His current research interests focus on high-energy solid-state batteries and electrochemical lithium extraction.

Yuan Menglei received his B.E. degree from North University of China in 2017. He then pursued his Ph.D. at the Institute of Process Engineering, Chinese Academy of Sciences, from 2017 to 2022. He joined the School of Materials Science and Engineering at Northwestern Polytechnical University (NPU) as an Associate Professor in 2022. He has published over 30 papers as first/corresponding author in journals such as J. Am. Chem. Soc., Angew. Chem. Int. Ed., Adv. Mater., with over 3,000 citations and an H-index of 31. His current research interests focus on electrocatalytic small molecule activation and organic electrosynthesis for the production of high-value chemicals such as ammonia, urea, amides, and olefins.

Hu Jiaxin received her B.E. degree from Sichuan University in 2023 and her M.S. degree from Nanyang Technological University in 2026, both in Materials Science and Engineering. Her research interests focus on electrochemical energy conversion and storage, including electrocatalysis, battery materials, and computational studies of electrochemical interfaces. She utilizes density functional theory (DFT) calculations and experimental approaches to investigate structure property relationships, electronic structures, and reaction mechanisms in advanced electrochemical systems. Her current research focuses on rational material design, interfacial regulation, and the development of efficient electrochemical materials for sustainable energy applications.